Diagnosing scale-dependent energy cycles in a high-resolution isopycnal ocean model

Nora Loose,[a] Scott Bachman,[b] Ian Grooms,[a] Malte Jansen[c]

[a] *Department of Applied Mathematics, University of Colorado, Boulder, CO 80309*
[b] *Climate and Global Dynamics Laboratory, National Center for Atmospheric Research, Boulder, CO 80301*
[c] *Department of the Geophysical Sciences, The University of Chicago, Chicago, IL 60637*

ABSTRACT: Energy exchanges between large-scale ocean currents and mesoscale eddies play an important role in setting the large-scale ocean circulation but are not fully captured in models. To better understand and quantify the ocean energy cycle, we apply along-isopycnal spatial filtering to output from an isopycnal 1/32° primitive equation model with idealized Atlantic and Southern Ocean geometry and topography. We diagnose the energy cycle in two frameworks: (1) a non-thickness-weighted framework, resulting in a Lorenz-like energy cycle, and (2) a thickness-weighted framework, resulting in the Bleck energy cycle. This paper shows that (2) is the correct framework for studying energy pathways when an isopycnal average is used. Next, we investigate the Bleck cycle as a function of filter scale. Baroclinic conversion generates mesoscale eddy kinetic energy over a wide range of scales, and peaks near the deformation scale at high latitudes, but below the deformation scale at low latitudes. Away from topography, an inverse cascade transfers kinetic energy from the mesoscales to larger scales. The upscale energy transfer peaks near the energy-containing scale at high latitudes, but below the deformation scale at low latitudes. Regions downstream of topography are characterized by a downscale kinetic energy transfer, in which mesoscale eddies are generated through barotropic instability. The scale- and flow-dependent energy pathways diagnosed in this paper provide a basis for evaluating and developing scale- and flow-aware mesoscale eddy parameterizations.

SIGNIFICANCE STATEMENT: Blowing winds provide a major energy source for the large-scale ocean circulation. A substantial fraction of this energy is converted to smaller-scale eddies, which swirl through the ocean as sea cyclones. Ocean turbulence causes these eddies to transfer part of their energy back to the large-scale ocean currents. This ocean energy cycle is not fully simulated in numerical models, but plays an important role in transporting heat, carbon, and nutrients throughout the world's oceans. The purpose of this study is to quantify the ocean energy cycle by using fine-scale idealized numerical simulations of the Atlantic and Southern Oceans. Our results provide a basis for how to include unrepresented energy exchanges in coarse global climate models.

1. Introduction

The ocean is a turbulent fluid, in which motions on a wide range of scales–from thousands of kilometers to centimeters–interact and exchange energy. One major cross-scale energy transfer is through baroclinic instability, a process that extracts potential energy from the large-scale ocean currents and generates mesoscale eddies near the scale of the deformation radius, at horizontal scales of tens to hundreds of kilometers (Charney 1947; Eady 1949; Gill et al. 1974). Quasi-geostrophic (QG) turbulence theory predicts that an inverse cascade transfers kinetic energy from the mesoscales back to the large-scale flow. Energy exchanges in the real ocean are more complex than in the picture described above. For instance, interactions with topography and loss of balance can trigger a forward energy cascade, in which eddy energy is fluxed downscale rather than upscale (e.g., Molemaker et al. 2010; Gula et al. 2016).

The ocean energy cycle remains challenging to constrain with observations, due to their limited spatial and temporal coverage (Ferrari and Wunsch 2009). To better understand and quantify energy exchanges across scales, previous studies have diagnosed the ocean energy cycle in numerical models, and four-box energy diagrams have proven as a useful framework (e.g., Aiki and Richards 2008; von Storch et al. 2012; Chen et al. 2014; Kang and Curchitser 2015; Barthel et al. 2017). These diagrams consist of four energy reservoirs: mean potential energy (MPE), mean kinetic energy (MKE), eddy potential energy (EPE), and eddy kinetic energy (EKE). The energy exchanges between these four reservoirs crucially depend on how the mean velocity is defined, and two main approaches have been pursued. A Eulerian mean formulation leads to a Lorenz energy diagram (Lorenz 1955), while a thickness-weighted (or residual) mean velocity formulation leads to a Bleck energy diagram (Bleck 1985). One major difference between these two diagram types is the cross-scale energy transfer associated with baroclinic instability (Plumb 1983; Aiki and Richards 2008). In the Lorenz diagram, baroclinic instability takes the potential energy route: the energy transferred from the large scales to the mesoscales originates in the MPE reservoir. This energy route is consistent with the picture that mesoscale eddies flatten isopycnals of the large-scale

Corresponding author: Nora Loose, nora.loose@colorado.edu

currents, thus extracting large-scale potential energy. In the Bleck diagram, baroclinic instability follows the kinetic energy route, where the cross-scale energy transfer originates in the MKE (rather than the MPE) reservoir. This energy pathway is consistent with another effect that mesoscale eddies have on the large-scale flow: they vertically redistribute geostrophic momentum.

The Lorenz and Bleck energy diagrams are closely linked to two distinct approaches to parameterize the effect of baroclinic instability and mesoscale eddies in ocean models. The Gent and McWilliams (1990) parameterization introduces an eddy term in the tracer (and thickness) equation, mimicking the extraction of MPE by mesoscale eddies, consistent with the Lorenz diagram. On the other hand, the Greatbatch and Lamb (1990) parameterization places the eddy term in the momentum equation, modifying the MKE reservoir by vertically redistributing geostrophic momentum, consistent with the Bleck diagram. Their close link to the Gent and McWilliams (1990) and Greatbatch and Lamb (1990) parameterizations make the Lorenz and Bleck diagrams particularly useful for evaluating whether these two mesoscale parameterizations extract energy from the large-scale flow at the correct rate. One objective of this work is to derive and compare the two energy diagrams in an isopycnal model, with the eventual goal to evaluate and improve mesoscale eddy parameterizations.

To make the Lorenz and Bleck energy diagrams most suitable for diagnosing energy exchanges across spatial scales and for evaluating mesoscale eddy parameterizations for a range of different horizontal model resolutions, the definition of the mean and eddy energy reservoirs should be tied to a spatial scale. Even still, most studies that have investigated ocean models' energy cycles or cross-scale energy transfers have defined 'mean' and 'eddies' in terms of a temporal Reynolds average (e.g., Aiki and Richards 2008; von Storch et al. 2012; Chen et al. 2014; Kang and Curchitser 2015; Barthel et al. 2017), or an ensemble average (e.g., Ajayi et al. 2021), with the exception of few studies (e.g., Grooms et al. 2013; Aluie et al. 2018), who investigated cross-scale energy transfers using a spatial filter. In this paper, we present *scale-dependent* energy diagrams, where we replace the frequently used temporal Reynolds average by a spatial filter.

In summary, this work has two main objectives:

1. To derive and compare the Lorenz and Bleck energy cycles in an isopycnal model;

2. To explore the energy cycle as a function of scale.

To achieve these goals, we use output from a 1/32° primitive equation model with intermediate idealization (Marques et al. 2022) and a spatial filtering operator (Grooms et al. 2021) with different horizontal scales (from 0.5° to 4°). In a follow-up paper we will use our diagnosed scale-dependent energy cycles to evaluate mesoscale eddy parameterizations.

2. Methods

a. Model configuration

We analyze output from an idealized 1/32° MOM6 simulation in the NeverWorld2 configuration (Marques et al. 2022). NeverWorld2 uses a regular latitude/longitude grid. The domain spans a single basin of 4000 m depth that extends over both hemispheres and has a re-entrant channel in the Southern Hemisphere (Figure 1(a)). The circumpolar channel is interrupted by a semi-circular ridge of 2000 m height, which is meant to mimic the Scotia Arc across the Drake Passage. A broad abyssal ridge of 2000 m height runs from north to south in the middle of the basin, and represents an idealized mid-Atlantic ridge.

NeverWorld2 uses a stacked shallow water model formulation with $N = 15$ layers. The top layer is indexed by $n = 1$, and the bottom layer by $n = N$. The thickness and velocity equations in layer n are given by

$$\partial_t h_n + \nabla \cdot (h_n \boldsymbol{u}_n) = 0, \tag{1}$$

$$\partial_t \boldsymbol{u}_n + \frac{f + \zeta_n}{h_n} \hat{\boldsymbol{z}} \times (h_n \boldsymbol{u}_n) + \nabla K_n = -\nabla M_n + \boldsymbol{F}_n^v + \boldsymbol{F}_n^h, \tag{2}$$

where h_n is the layer thickness, ∇ the two-dimensional gradient operator, $\boldsymbol{u}_n = (u_n, v_n)$ the horizontal velocity, f the Coriolis parameter, $\zeta_n = \hat{\boldsymbol{z}} \cdot (\nabla \times \boldsymbol{u}_n)$ the relative vorticity, $K_n = |\boldsymbol{u}_n|^2/2$ the kinetic energy density, and $M_n = \sum_{k=0}^{n-1} g'_k \eta_k$ the Montgomery potential. In the Montgomery potential, $g'_k = g(\rho_{k+1} - \rho_k)/\rho_o$ and $\eta_k = -D + \sum_{i=k+1}^{N} h_i$ denote the reduced gravity and the interface height between layer k and $k+1$, respectively. ρ_o is the reference density, and D denotes the ocean depth shown in Figure 1(a). Finally, $\boldsymbol{F}_n^v$ and $\boldsymbol{F}_n^h$ are the vertical and horizontal friction terms in the velocity equation.

The vertical friction term $\boldsymbol{F}_n^v$ contains the effects of wind forcing, vertical viscosity, and bottom drag. The surface stresses are applied as a uniform body-force distributed over the top boundary layer of specified thickness. Marques et al. (2022) describe NeverWorld2 simulations where the top boundary layer is defined to have a thickness of 5 m. Here, we analyze a modified NeverWorld2 simulation, where the top boundary layer is defined to be deeper: 20 m rather than 5 m. This is the only aspect in which the model setup for the simulation

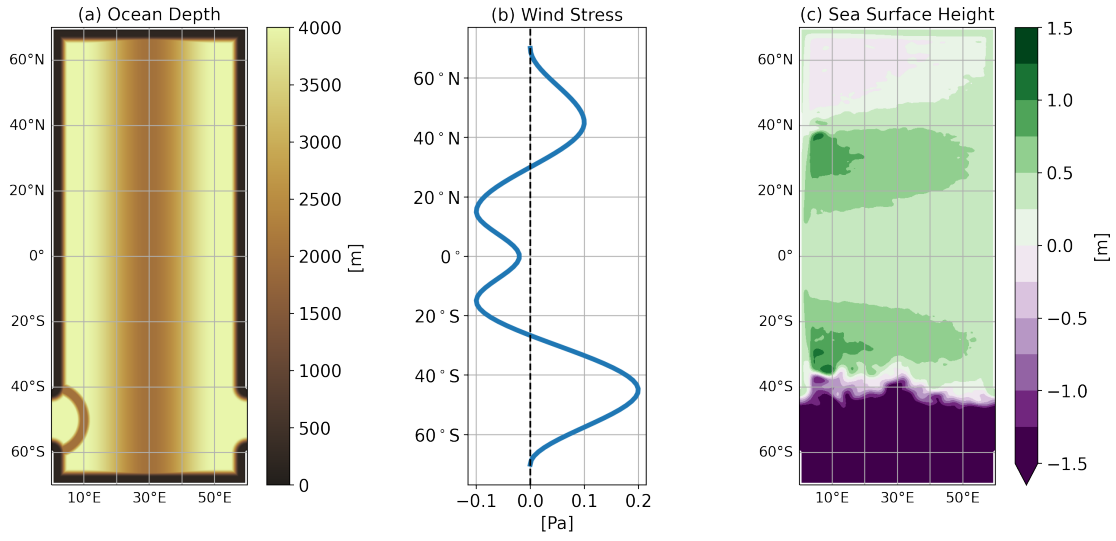

FIG. 1. NeverWorld2 configuration and flow: (a) ocean depth, (b) fixed zonal wind stress, and (c) 500-day averaged sea surface height (SSH). The SSH gradients in (c) reveal the major circulation patterns: a circumpolar jet in the Southern Hemisphere, subtropical gyres in both hemispheres, and a subpolar gyre in the Northern Hemisphere.

analyzed in this paper differs from the one described in Marques et al. (2022). We use the modified NeverWorld2 simulation because we found that a deeper top boundary layer leads to more realistic dissipation pathways, with more kinetic energy being dissipated via bottom drag rather than via horizontal friction.

The surface wind stress is prescribed and fixed in time, with a zonally constant profile (Figure 1(b)). The bottom stress uses a quadratic drag law. The horizontal friction term $\boldsymbol{F}_n^h$ is given by the biharmonic Smagorinsky closure (Griffies and Hallberg 2000) with a resolution-dependent background viscosity. More details on the 1/32° NeverWorld2 configuration can be found in Marques et al. (2022).

b. Total energy budgets

In this work, we study conversions between depth-integrated energy reservoirs. Before decomposing the energy reservoirs into their mean and eddy components, we consider the total (undecomposed) energy budgets. The depth-integrated potential energy (PE) is given by

$$\mathrm{PE} = \sum_{n=0}^{N-1} \mathrm{PE}_n = \frac{1}{2} \sum_{n=0}^{N-1} g'_n \eta_n^2, \tag{3}$$

and the depth-integrated kinetic energy (KE) by

$$\mathrm{KE} = \sum_{n=1}^{N} \mathrm{KE}_n = \frac{1}{2} \sum_{n=1}^{N} h_n |\boldsymbol{u}_n|^2. \tag{4}$$

The summation in equations (3) and (4) goes from 0 to $N-1$ and from 1 to N, respectively, because PE is defined at layer interfaces while KE is defined at layer midpoints. Using the continuity equation (1), the product rule, and summing over all layers, we obtain the following evolution equation for depth-integrated PE:

$$\begin{aligned} \partial_t \left(\sum_{n=0}^{N-1} \mathrm{PE}_n \right) &= \sum_{n=0}^{N-1} g'_n \eta_n \partial_t \eta_n = - \sum_{n=0}^{N-1} g'_n \eta_n \sum_{i=n+1}^{N} \nabla \cdot (\boldsymbol{u}_i h_i) \\ &= - \sum_{n=1}^{N} M_n \nabla \cdot (h_n \boldsymbol{u}_n). \end{aligned} \tag{5}$$

We obtain the KE equation for layer n by multiplying the continuity equation (1) by $|\boldsymbol{u}_n|^2$, taking the dot of $h_n \boldsymbol{u}_n$ with the velocity equation (2), and adding the two:

$$\begin{aligned} \partial_t (\mathrm{KE}_n) = &- \nabla \cdot (\boldsymbol{u}_n \mathrm{KE}_n) - h_n \boldsymbol{u}_n \cdot \nabla M_n \\ &+ h_n \boldsymbol{u}_n \cdot \boldsymbol{F}_n^v + h_n \boldsymbol{u}_n \cdot \boldsymbol{F}_n^h. \end{aligned} \tag{6}$$

The equation for depth-integrated KE is simply obtained by summing (6) over all layers.

c. Spatial filtering

To diagnose energy cycles that are scale-dependent, we apply a spatial filter to 5-day averaged NeverWorld2 data. We use the python package `gcm-filters` (Loose et al. 2022) whose underlying algorithm applies a discrete Laplacian to smooth a field through an iterative process that resembles diffusion (Grooms et al. 2021). For the purpose of filtering, we treat the zonal and meridional

components of a vector field in the same way as scalar fields, and apply a diffusion-based filter to each of the vector components separately (rather than applying a viscosity-based filter to the full vector field, see Grooms et al. (2021)). We choose a Gaussian filter shape, which results in a filter that resembles (but not equals) a Gaussian convolution kernel. The filter employs a no-flux boundary condition, ensuring conservation of the integral.

We filter our 1/32° NeverWorld2 data to four different horizontal resolutions: 0.5°, 1°, 2°, and 4°. These filter scales are meant to broadly reflect effective resolutions of eddy-permitting to non-eddying global ocean models. While today's global ocean models have grid scales that are typically finer than what is represented by the range of our filter scales, past studies have argued that a model's effective resolution is larger than its grid scale by a factor of anywhere between 2 and 20 (Skamarock 2004; Kent et al. 2014; Soufflet et al. 2016).

To achieve any of our four target filter resolutions, the filter scale needs to be defined as a fixed coarsening factor (16, 32, 64, 128, respectively) times the local grid scale. Tying the filter scale to the spatially-varying local grid scale, rather than choosing a fixed filter length scale of for example 100 km, seems most relevant for the evaluation of mesoscale eddy closures in ocean models. However, a spatially varying filter scale comes at a cost: spatial derivatives do not commute with the filter (Grooms et al. 2021), though time derivatives still do. We will account for the lack of commutativity in the derivation of our energy diagrams.

d. Energy reservoirs & diagrams

We derive energy diagrams in two distinct frameworks: in a non-thickness-weighted averaged (non-TWA) framework, and in a thickness-weighted averaged (TWA) framework.

The definition of the mean and eddy potential energy reservoirs is the same in these two frameworks:

$$\mathrm{MPE} = \frac{1}{2}\sum_{n=0}^{N-1} g'_n \overline{\eta}_n^2, \tag{7}$$

$$\mathrm{EPE} = \overline{\mathrm{PE}} - \mathrm{MPE}, \tag{8}$$

where overbars denote a spatial filter applied along isopycnals and on 5-day averaged data. We would like to emphasize two points related to the overbar (our 'mean'), both of which hold true throughout this paper. First, filtering along isopycnals is distinct from an Eulerian average or filter; the latter filter is applied at constant depth. Second, our overbar is not only a spatial filter, but more accurately the composition of a 5-day mean (i.e., a temporal filter) and a spatial filter.

The definition in (8) ensures that there is an exact decomposition of the total energy reservoir, $\overline{\mathrm{PE}}$, into its mean and eddy components. Similarly, we will enforce an exact decomposition of $\overline{\mathrm{KE}}$ into the MKE and EKE reservoirs. The way in which this decomposition is performed differs between the non-TWA and TWA frameworks.

1) Non-TWA framework

In the non-TWA framework, the mean and eddy kinetic energy reservoirs are defined as

$$\mathrm{MKE} = \frac{1}{2}\sum_{n=1}^{N} \overline{h}_n |\overline{\boldsymbol{u}}_n|^2, \tag{9}$$

$$\mathrm{EKE} = \overline{\mathrm{KE}} - \frac{1}{2}\sum_{n=1}^{N} \overline{h}_n |\overline{\boldsymbol{u}}_n|^2, \tag{10}$$

where the overbar denotes the same along-isopycnal filter as before. Figure 2 show MKE and EKE for the case in which equations (9) and (10) use a spatial filter with filter scale 1°. Figures 2(a),(b) present MKE and EKE for an arbitrary 5-day interval, while Figures 2(c),(d) show zonally and meridionally integrated $\langle \mathrm{MKE} \rangle$ and $\langle \mathrm{EKE} \rangle$, where $\langle \cdot \rangle$ denotes a 500-day average, and the meridional integral spans the latitudes of the circumpolar channel. The fact that MKE is at least twice as large as EKE (Figures 2(c),(d)) re-emphasizes that the filter scale does not directly translate to the grid scale of a coarse model. Indeed, a coarse non-eddying model of grid size 1° is not expected to resolve most of the KE.

A vigorous mean and eddy kinetic energy field is present in the circumpolar channel between 40°S and 60°S, but also in the western part between 30°S and 40°S, where the circumpolar flow sharply recirculates downstream of Drake Passage (Figures 2(a)-(c)). Within the channel, the flow is most energetic downstream of the topographic features: downstream of Scotia Arc between 10°E and 20°E, and downstream of the mid-Atlantic ridge between 45°E and 50°E (Figures 2(d),(e)). Near 40°N a jet separates from the western boundary, similar to the Gulf Stream (cf. Figure 1(c)), and both its mean and eddy components are energetic. The equatorial region is characterized by high MKE but low EKE (Figures 2(a)-(c)), indicative of generally larger-scale flows. In the mid-latitudes, another notable energetic region is centered at ±15°N (Figures 2(a)-(c)), which is characterized by the westward subtropical return flows (cf. Figure 1(c)).

Figure 3(a) shows the energy diagram derived in the non-TWA framework (Appendices A1, A2), and the energy pathways can be thought of as follows. Large-scale

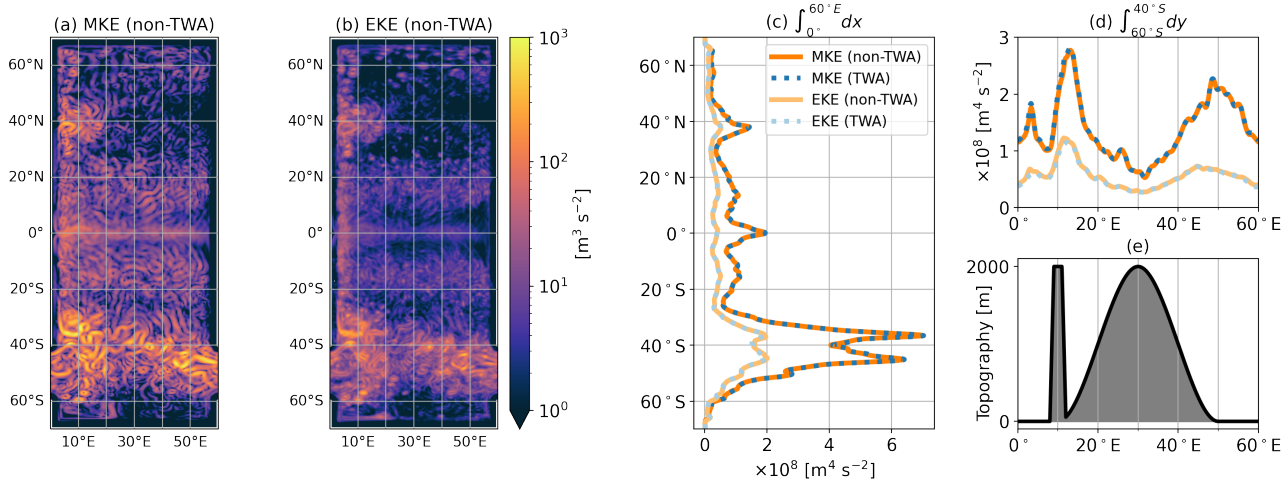

FIG. 2. (a),(b) Mean kinetic energy (MKE) and eddy kinetic energy (EKE) in the non-TWA framework for an arbitrary 5-day interval. (c),(d) 500-day averaged, zonally and meridionally integrated MKE and EKE in the non-TWA and TWA frameworks and, where the meridional integral in (d) spans across the latitudes of the circumpolar channel. (a)-(d) use a filter scale of 1°. (e) Topography along the latitude band of 50°S.

wind-driven Ekman pumping builds up and maintains a large reservoir of MPE (green arrow). The large-scale ocean currents are unstable to baroclinic instability, eventually converting MPE to EKE (red arrows). The work done by eddy momentum fluxes, Π^L, can transfer energy between MKE and EKE in either direction (blue arrow).

Our non-TWA diagram in Figure 3(a) resembles the Lorenz diagram (Lorenz 1955), but we emphasize that we have used isopycnal averaging, while the classical Lorenz diagram is derived via Eulerian averaging. We hereafter refer to our non-TWA energy cycle as a 'Lorenz-like' energy cycle.

2) TWA FRAMEWORK

In the previous section, the mean velocity was defined by simply applying the spatial filter to $\boldsymbol{u}_n$. In the TWA framework we instead define the mean velocity as

$$\hat{\boldsymbol{u}}_n = \frac{\overline{h_n \boldsymbol{u}_n}}{\bar{h}_n}; \tag{11}$$

that is, the spatial filter is applied to the thickness-multiplied velocity $h_n \boldsymbol{u}_n$, and the result is divided by the filtered thickness. Thickness and KE are filtered as before.

With this definition of the mean velocity, the kinetic energy reservoirs are now specified as

$$\mathrm{MKE} = \frac{1}{2}\sum_{n=1}^{N} \overline{h}_n |\hat{\boldsymbol{u}}_n|^2, \tag{12}$$

$$\mathrm{EKE} = \overline{\mathrm{KE}_n} - \frac{1}{2}\sum_{n=1}^{N} \overline{h}_n |\hat{\boldsymbol{u}}_n|^2. \tag{13}$$

Despite the distinct definition of the MKE and EKE reservoirs compared to the non-TWA framework, their distribution is virtually identical (Figures 2(c),(d)).

While the sizes of the energy reservoirs are indistinguishable in the non-TWA and TWA frameworks, the energy pathways between the reservoirs are inherently different. Figure 3(b) shows the energy diagram derived in the TWA framework (Appendices A1, A2), and the energy pathways can be thought of as follows. The wind-induced overturning (green arrow) is counteracted by the work of the bolus velocity $\boldsymbol{u}_n^{\mathrm{bolus}} = \hat{\boldsymbol{u}}_n - \bar{\boldsymbol{u}}_n$ (red arrow between MPE and MKE), where the latter is included as part of the residual mean velocity $\hat{\boldsymbol{u}}_n$ in the TWA framework. The baroclinic instability pathway follows the kinetic energy route, associated with a vertical redistribution of momentum, and eventually transfers MKE to EKE (red arrows). Π^B represents the lateral (rather than the vertical) redistribution of momentum by eddies, and can transfer energy between MKE and EKE in either direction (blue arrow).

The diagram in Figure 3(b) is the Bleck diagram (Bleck 1985), and is similar to the one derived by Aiki et al. (2015), except that the diagram here is for a stacked shallow wa-

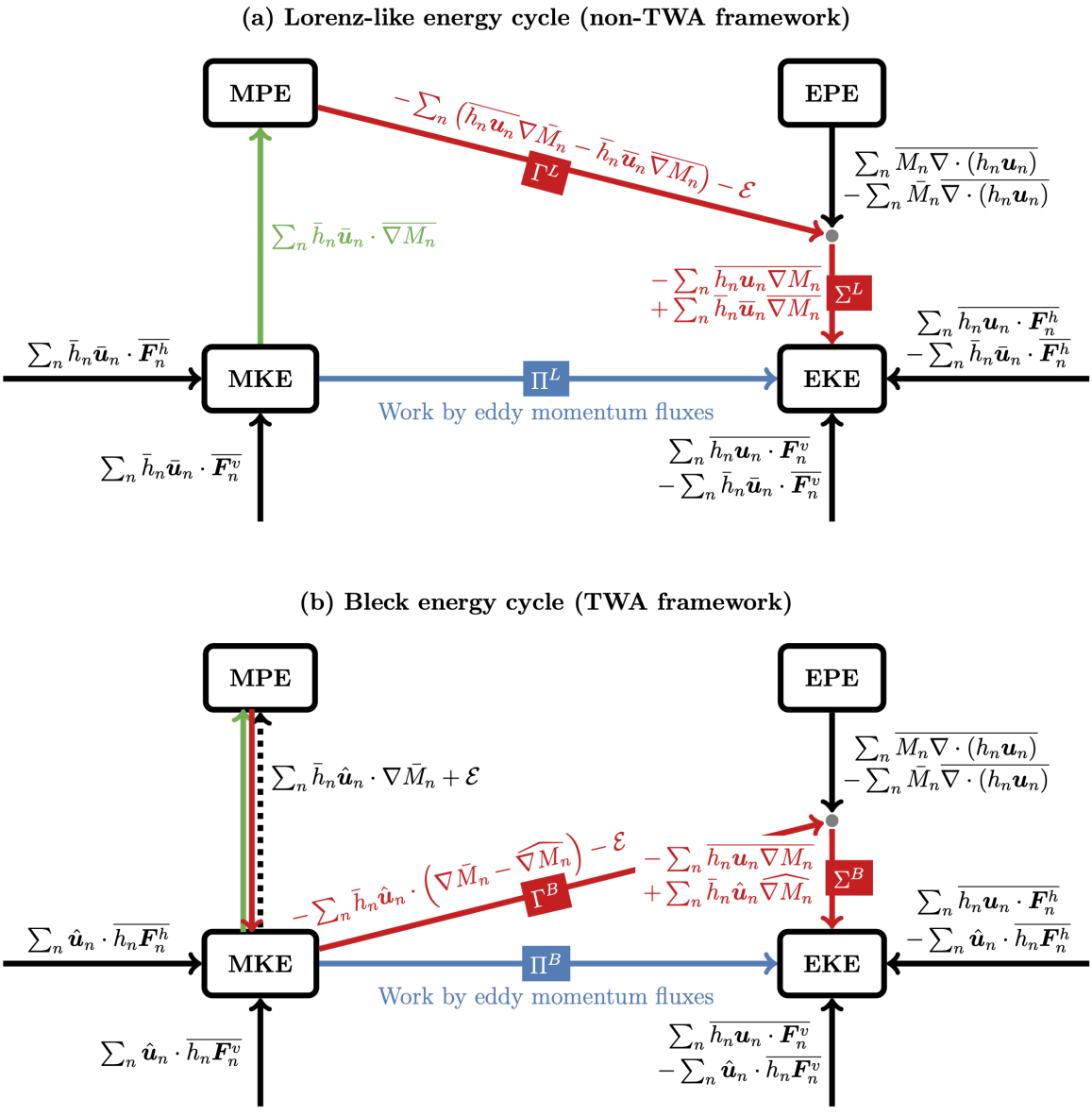

FIG. 3. Energy diagrams that are obtained using an along-isopycnal filter in the (a) non-TWA and (b) TWA frameworks. Green arrows: energy conversions associated with Ekman pumping. Red arrows: energy conversions associated with baroclinic instability. Blue arrows: energy conversions associated with eddy momentum fluxes (equations (A9), (A16)). The term $\mathcal{E}$ (equation (A4)) is an extra term that arises due to the fact that the filter does not commute with spatial derivatives. The three arrows that meet at the gray circle between the EPE and EKE reservoirs in either diagram only differ by a flux divergence (equations (A13), (A12), (A19)), which integrates to zero over the domain.

ter system with more than just two layers. Moreover, we use a spatial filter, rather than a temporal Reynolds average. Non-commutation of our spatial filter with derivatives leads to extra terms in our diagram, such as $\mathcal{E}$ (equation (A4)).

3. Comparing the Lorenz and Bleck energy cycles

This section compares the Lorenz-like and Bleck energy cycles for our NeverWorld2 data. To simplify the presentation, we only show results for one of our four filter scales: 1°. We will vary the filter scale in section 4.

a. Wind work and dissipation

We first examine the external sources and sinks in our energy cycles. NeverWorld2 does not include any surface buoyancy fluxes, so external sources and sinks of energy act exclusively on the MKE and EKE reservoirs via the horizontal and vertical stresses, $\boldsymbol{F}_n^h$ and $\boldsymbol{F}_n^v$ (Figure 3). The vertical stresses can be further decomposed into contributions by wind stress, bottom drag, and vertical friction:

$$\boldsymbol{F}_n^v = \boldsymbol{F}_n^{\text{wind}} + \boldsymbol{F}_n^{\text{drag}} + \boldsymbol{F}_n^{\text{visc}}.$$

The stresses $\boldsymbol{F}_n^v$ and $\boldsymbol{F}_n^{\text{wind}}$, along with their thickness-weighted versions ($h_n\boldsymbol{F}_n^v$ and $h_n\boldsymbol{F}_n^{\text{wind}}$) and energetic effects ($h_n\boldsymbol{u}_n \cdot \boldsymbol{F}_n^v$ and $h_n\boldsymbol{u}_n \cdot \boldsymbol{F}_n^{\text{wind}}$), are model diagnostics that are computed online and output as 5-day averages. We separate the remainders $\boldsymbol{F}_n^v - \boldsymbol{F}_n^{\text{wind}}$, $h_n(\boldsymbol{F}_n^v - \boldsymbol{F}_n^{\text{wind}})$, and $h_n\boldsymbol{u}_n \cdot (\boldsymbol{F}_n^v - \boldsymbol{F}_n^{\text{wind}})$ offline into bottom drag and vertical friction contributions, by classifying them as a contribution by bottom drag if the lower interface of layer n is within 5 m from the bottom, and as a contribution by vertical friction otherwise.[1]

The work done by either of the four stresses $\boldsymbol{F}^h$, $\boldsymbol{F}^{\text{wind}}$, $\boldsymbol{F}^{\text{drag}}$, and $\boldsymbol{F}^{\text{visc}}$ on the total KE reservoir, i.e., the MKE and EKE reservoirs taken together, is the same in the non-TWA and TWA frameworks (Figure 3). It is given by $\sum_{n=1}^{N} \overline{h_n\boldsymbol{u}_n \cdot \boldsymbol{F}_n^*}$, for $* \in \{h, \text{wind}, \text{drag}, \text{visc}\}$, and is shown in Figures 4(a)-(d) as a 500-day average. The wind provides a large source of energy in the circumpolar channel and to a lesser extent in the gyres (Figure 4(a)). The channel is also the region where bottom drag, vertical and horizontal friction dissipate the largest amounts of energy (Figures 4(b)-(d)). The domain integrals of the energy sources and sinks in Figures 4(a)-(d) are shown by the black bars in Figures 4(e)-(h). (Note that these integrals are equal to the integrals of the respective *unfiltered* work, $\sum_{n=1}^{N} h_n\boldsymbol{u}_n \cdot \boldsymbol{F}_n^*$, because our spatial filter conserves the domain integral.) Bottom drag acts as the major KE sink, while horizontal and vertical friction dissipate a much smaller fraction of the total KE.

Figure 4(e) and Figures 5(a)-(d) show the decomposition of total wind work into wind work on mean flow vs. eddies in the non-TWA and TWA frameworks. In the TWA framework, the wind work acts almost entirely on the large-scale mean flow (blue bars in Figure 4(e), and Figures 5(c),(d)), as expected. In contrast, in the non-TWA framework, wind work on the mean flow overshoots wind work on the total flow such that the wind acts as an energy sink on the non-TWA eddies (orange bars in Figure 4(e), and Figures 5(a),(b)). Eddy killing by wind is a phenomenon observed in the real ocean (Rai et al. 2021) but is not expected in NeverWorld2, which uses a wind stress that is independent of the ocean currents (Duhaut and Straub 2006; Renault et al. 2016).

The peculiar and unphysical decomposition of total wind work in the non-TWA framework shown in Figure 4(e) and Figures 5(a),(b) is a spurious effect of using an isopycnal non-thickness-weighted average. Wind stress $\boldsymbol{F}_n^{\text{wind}}$ and layer thickness h_n are anticorrelated (in both space and time) for layers that straddle the lower interface of the boundary layer over which the wind stress is distributed. Figure 5(g) illustrates the spatial anticorrelation between $\boldsymbol{F}_n^{\text{wind}}$ and h_n for layer $n = 7$ and an arbitrary 5-day time interval. The anticorrelation is captured by the wind work on the TWA mean flow, $\hat{\boldsymbol{u}}_n\overline{h_n\boldsymbol{F}_n^{\text{wind}}}$ (Figure 3(b)). In contrast, the wind work on the non-TWA mean flow, $\bar{h}_n\bar{\boldsymbol{u}}_n\overline{\boldsymbol{F}_n^{\text{wind}}}$ (Figure 3(a)), misses this anticorrelation, which results in the observed overshooting of the total wind work (orange bar, Figure 4(e)). The excessive wind work on the non-TWA mean flow goes in tandem with unphysical eddy killing by wind (blue shading in layers 6 and 7 in Figure 5(e)), which results from the introduction of a spurious "eddy Ekman transport" contribution, even in the presence of a constant wind stress.

The spurious eddy killing by wind is not the result of using a spatial filter; it would arise similarly if we used an along-isopycnal non-thickness-weighted temporal Reynolds average rather than a spatial filter (Figure 5(f)). The explanation is that $\boldsymbol{F}_n^{\text{wind}}$ and h_n are anticorrelated in time, space, and even across ensembles. In summary, computing non-TWA diagnostics along isopycnals leads to spurious results.

The unphysical nature of non-TWA wind work, which was investigated in Figure 5, materializes similarly for the work done by vertical friction. Vertical friction $\boldsymbol{F}_n^{\text{visc}}$ and layer thickness h_n show anticorrelation in layers that straddle the lower interface of the mixed layer over which vertical viscosity in enhanced. As before, the non-TWA term $\bar{h}_n\bar{\boldsymbol{u}}_n\overline{\boldsymbol{F}_n^{\text{visc}}}$ (Figure 3(a)) misses this anticorrelation, and the work of vertical friction on the non-TWA mean flow overshoots the total vertical friction work in amplitude (Figure 4(g)). Consequently, the vertical friction work on the non-TWA eddies is of opposite, i.e., *positive*, sign - clearly a spurious symptom of analyzing along-isopycnal non-TWA diagnostics.

Bottom drag is a sink for MKE and EKE, and acts mostly on the large scales, in both the non-TWA and TWA

[1]We have to make this approximation because the thickness of the bottom boundary layer was not saved as an online diagnostic. At locations where the bottom boundary layer is thicker than 5 m, our calculation may incorrectly attribute bottom drag to vertical friction contributions (which is potentially the case over the mid-Atlantic ridge within the channel, see Figures 4(b),(c)). However, the main conclusions from this study are insensitive to the details of this offline attribution calculation.

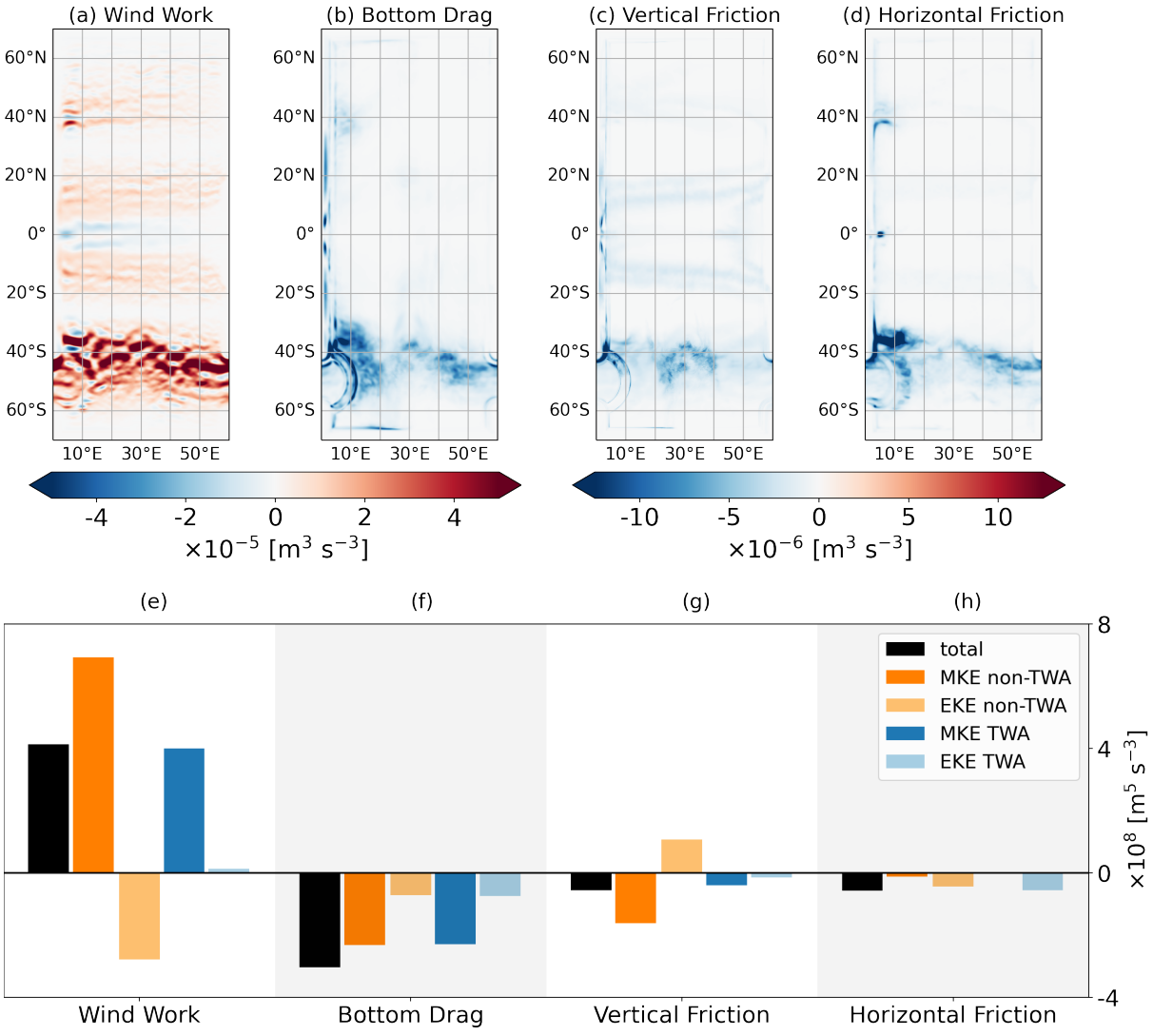

FIG. 4. (a)-(d) 500-day average of kinetic energy sources and sinks: (a) wind work, (b) bottom drag, (c) vertical friction, (d) horizontal friction. Note that the colorbar for (c),(d) is stretched by a factor of 4 compared to the colorbar for (a),(b). (e)-(h) The black bars show the spatial integrals of the terms in (a)-(d). The colored bars show how the total work (black bar) decomposes into work on the mean flow vs. eddies in the non-TWA and TWA frameworks (Figure 3), where all terms are integrated over the full domain and averaged over 500 days. All terms in this figure are for a filter scale of 1°.

frameworks (Figure 4(f)). There is no notable difference between the two frameworks because relative thickness variations of the bottom layer tend to be small.

Horizontal friction is expected to act predominantly on the small scales. This is a necessary criterion for studying inertial range dynamics, referred to as the *inviscid criterion* by Aluie (2013). In the TWA framework, the inviscid criterion is met: horizontal friction acts so dominantly on the EKE reservoir that its contribution to the MKE reservoir does not even appear (blue bars, Figure 4(h)). In the non-TWA framework, however, horizontal friction acts on both the MKE and EKE reservoirs (orange bars, Figure 4(h)), violating the inviscid criterion. The fact that the inviscid criterion is satisfied in a TWA framework but violated in a non-TWA framework is consistent with the theoretical predictions by Aluie (2013) and Zhao and Aluie (2018).

b. Routes of baroclinic instability

Figure 6 shows 500-day averages of the EKE production terms, Σ^L and Σ^B, that are associated with baroclinic instability (Figure 3). The largest energy source is found in the circumpolar channel, and to a lesser degree in the Gulf stream extension near 40°N as well as in the

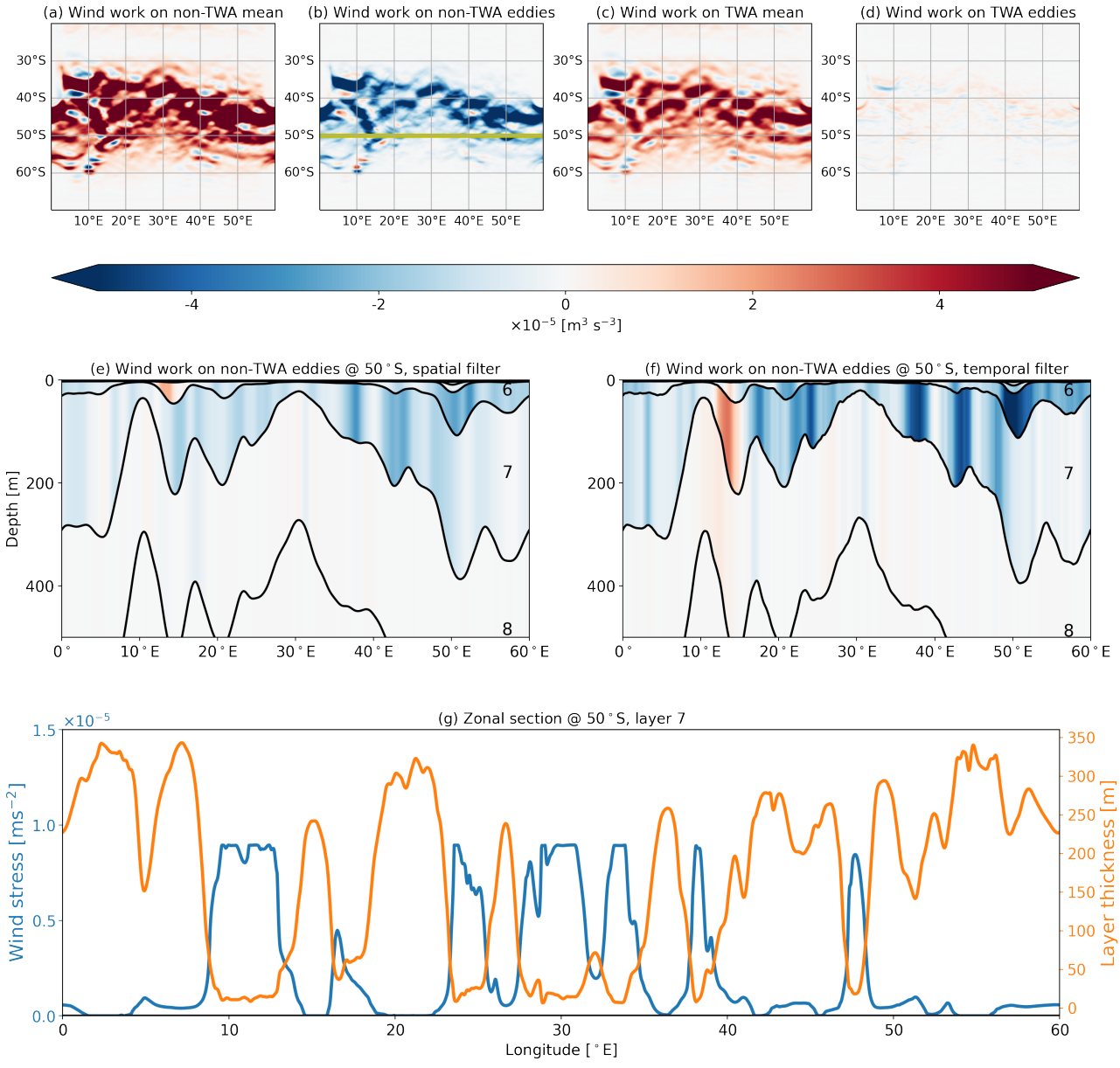

FIG. 5. (a)-(d) 500-day averages of wind work on mean flow and eddies in the non-TWA and TWA frameworks (Figure 3) for a filter scale of 1°, shown in the southern portion of the domain. The green line in (b) marks the cross-section at 50°S, which is further investigated in (e)-(g). (e) Wind work on non-TWA eddies (shading) as in (b), but now in longitude-depth space, along the latitude of 50°S and restricted to the upper 500 m. The contours show the layer interfaces, and the number on the right denotes the layer number (counted from the top downwards). (f) As (e), but re-computed with a temporal rather than a spatial filter: the overbar now denotes a 500-day average. The colorbar is shared by (a)-(f). (g) Wind stress $\boldsymbol{F}_n^{\text{wind}}$ (blue line) and layer thickness h_n (orange line) along the zonal section 50°S for $n = 7$ and an arbitrary 5-day interval.

subtropical return flows (Figures 6(a)-(c)). Within the channel, EKE production is increased downstream of topography, downstream of Scotia Arc between 10°E and 20°E and downstream of the mid-Atlantic ridge eastward of 30°E. There are a few isolated locations where Σ^L and Σ^B have negative sign, indicating that the eddies lose energy in the process of baroclinic conversion. A negative energy flux in a small portion of the domain is consistent with previous studies (e.g., Chen et al. 2014).

Up to a flux divergence and the EPE tendency (both of which are negligible when integrated over the domain), Σ^L and Σ^B are equal to the conversion terms Γ^L and Γ^B that leave the MPE and MKE reservoirs, respectively (Figure 3). Even though originating in distinct mean energy reservoirs, the horizontal distributions of Σ^L and Σ^B are

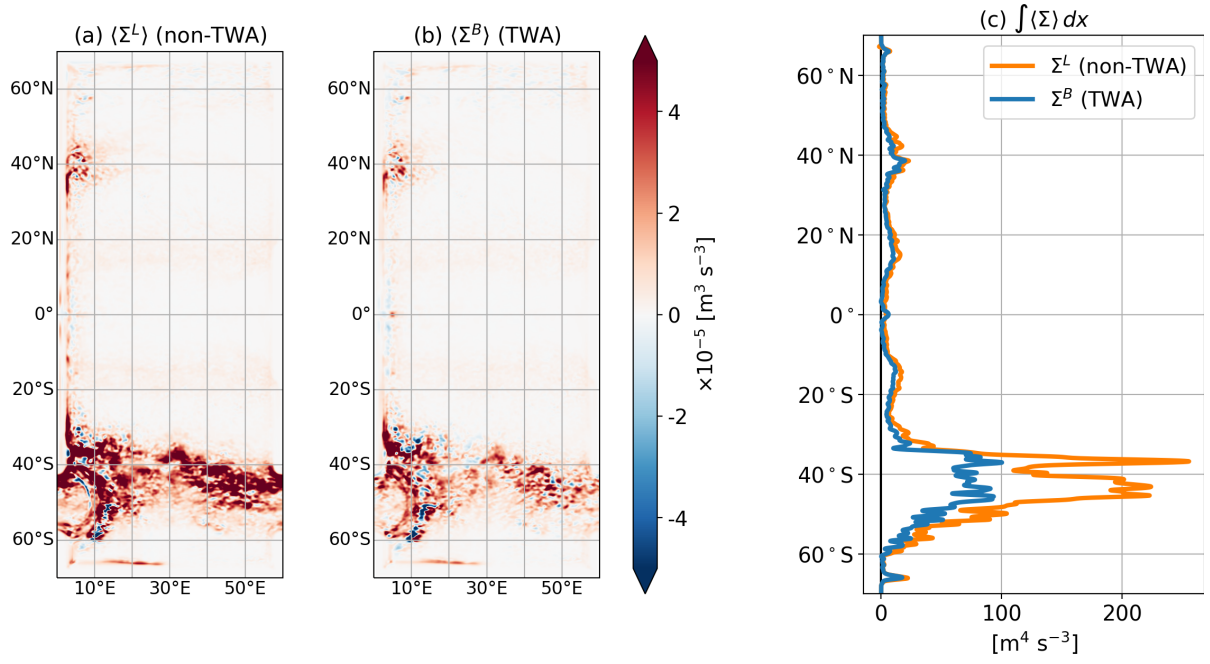

FIG. 6. EKE production by baroclinic instability, for a filter scale of 1°: (a) $\langle \Sigma^L \rangle$ in the non-TWA framework, and (b) $\langle \Sigma^B \rangle$ in the TWA framework, where $\langle \cdot \rangle$ denotes a 500-day average. (c) Zonal integral of the terms in (a) and (b).

broadly similar (Figures 6(a),(b)), with one important exception. A clear discrepancy can be seen in the channel where the values of Σ^L are enhanced by a factor of 2 to 3 compared to those of Σ^B (Figure 6(c)). The enhanced values of Σ^L are found near the surface (not shown). The superimposed surface signature is characterized by relatively large-scale features and resembles the horizontal distribution of the wind work on the non-TWA eddies (Figure 5(b)), but of opposite sign. This resemblance suggests that the high values in the non-TWA EKE production term largely balance the spurious non-TWA eddy killing, and are likely an unphysical side effect of using an along-isopycnal non-thickness-weighted average.

c. Work by eddy momentum fluxes

Figure 7 shows 500-day averages of the work done by eddy momentum fluxes, Π^L and Π^B, representing energy conversion between the MKE and EKE reservoirs through lateral redistribution of momentum. Positive values indicate that energy is converted from MKE to EKE through barotropic (or horizontal shear) instability. Negative values indicate that eddy momentum fluxes act to strengthen the mean flow, suggesting a KE inverse cascade.

The largest amplitudes of Π^L and Π^B are found in the channel (Figures 7(a)-(c)). Here, the terms have strong spatial variations with fluctuations between positive and negative values. Positive values are especially found downstream of topography: downstream of Scotia Arc near 10°E and downstream of the mid-Atlantic ridge between 30°E and 50°E. Enhanced barotropic instability downstream of topography, in tandem with enhanced MKE to EKE conversion, is consistent with the results in Barthel et al. (2017), who studied a two-layer ocean model with different topographic obstacles.

Centered at Scotia Arc, and to a lesser degree centered at 50°E, we see dipoles where Π^L and Π^B abruptly change sign from high-amplitude positive to high-amplitude negative values. At these locations, the respective EKE transport term (Equations (A10) and (A17)) has a dipole of the same sign (not shown). Our findings suggest the following chain of events. Barotropic instability releases energy to the eddies at (or just downstream of) topography. EKE is then transported downstream, where KE is transferred back from the eddies to the mean flow. This chain of events is consistent with the results from an idealized channel model in Youngs et al. (2017).

Outside of the channel, we observe a positive-negative dipole in Π^L and Π^B along the continental slope at the western boundary (Figures 7(a),(b)), again in concert with a dipole of the same sign in the EKE transport term (not shown). The chain of events described above applies for the western boundary current flowing over the continental slope as well. In the remainder of the domain, Π^L and Π^B have negative values suggestive of an inverse KE cascade, which is strongest in the separated Gulf Stream

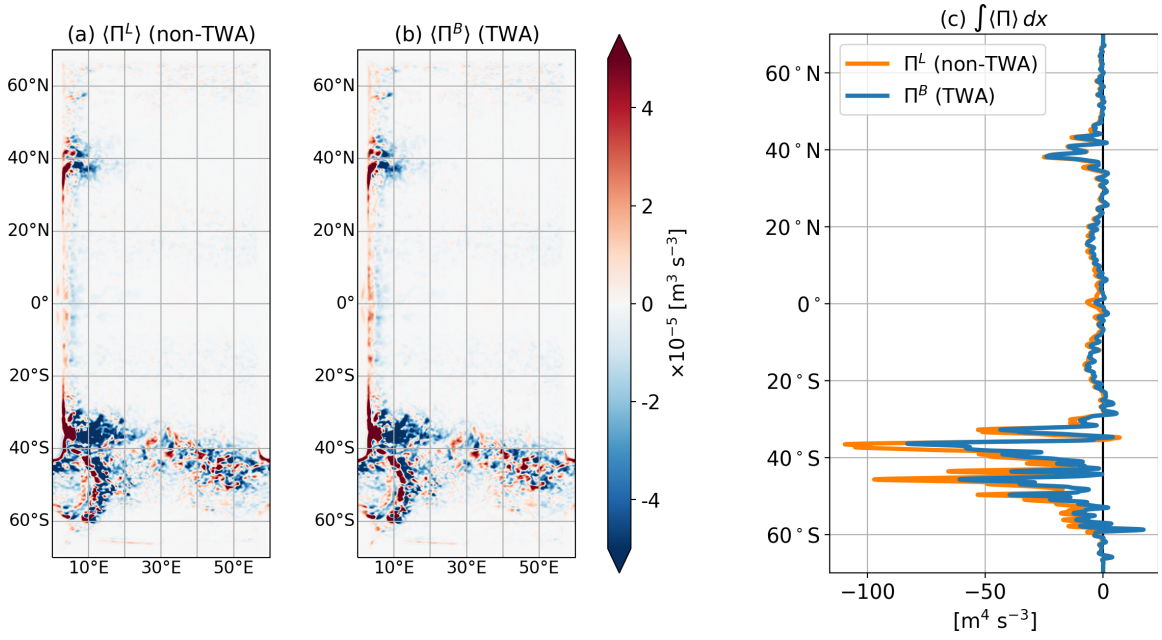

FIG. 7. Work done by the eddy momentum fluxes, for a filter scale of 1°: (a) $\langle \Pi^L \rangle$ in the non-TWA framework, and (b) $\langle \Pi^B \rangle$ in the TWA framework, where $\langle \cdot \rangle$ denotes a 500-day average. Positive values indicate that energy is converted from MKE to EKE through barotropic instability. Negative values indicate that eddy momentum fluxes act to strengthen the mean flow, suggesting a KE inverse cascade. (c) Zonal integral of the terms in (a) and (b).

near 40°N and the subtropical return flows centered at ±15°N (Figure 7(c)).

Comparing the spatial distributions of Π^L and Π^B suggests that the work done by eddy momentum fluxes is similar in the non-TWA vs. TWA frameworks (Figures 7(a)-(c)). We note that in the channel Π^L is higher in amplitude compared to Π^B (Figure 7(c)). It is unclear whether this difference is (partly) a side effect of Π^L having to balance the unphysical energetic effects of the vertical surface stresses on the MKE and EKE budgets, as it was the case for Σ^L (section 3b).

d. Summary of energy cycles

Figure 8 shows the domain-integrated energy conversion terms in the Lorenz-like and Bleck energy cycles (cf. Figure 3) averaged over 500 days, in units of GW. The cycles highlighted in gray (Figures 3(a),(c)) are for a filter scale of 1° and summarize the energy pathways discussed in this section. Adding up the values for the in- and outgoing arrows at each reservoir results in minor imbalances of up to 6 GW, which arise due to the energy reservoirs' tendencies, interpolation errors on the numerical grid, and rounding values to GW.

We note that the domain integral of $\mathcal{E}$ (equation (A4)), the term in Figure 3 arising from non-commutativity of filter and spatial derivatives, is small and rounds to 0 GW (not shown). However, the negligible energetic effect of $\mathcal{E}$ does not imply that the filter effectively commutes with spatial derivatives in all situations. Indeed, if we commuted our spatial filter with ∇M_n in the baroclinic conversions Γ^L and Γ^B (Figure 3) and computed $-\sum_n \overline{h_n \boldsymbol{u}_n}\ \overline{\nabla M_n}$ rather than $-\sum_n \overline{h_n \boldsymbol{u}_n} \nabla \bar{M}_n$, we would obtain baroclinic conversions that integrate to 34 GW less than the values shown by the diagonal red arrows in Figure 8. Accounting for non-commutativity of filter and derivatives–as we have done in Figure 3 and throughout this work–is therefore crucial.

The thick arrows in the Lorenz-like cycle (Figure 8(a)) indicate energy conversion terms that have unphysical (i.e., too large) values. In the case of EKE wind and vertical friction work (right green and orange arrows), the diagnosed work even points in the wrong direction. As discussed in section 3a, the unphysical values originate in applying an isopycnal non-thickness-weighted average. Figure 8(a) shows how the unphysical nature of the MKE and EKE source & sink terms discussed in section 3a propagates throughout the entire energy cycle. Indeed, the large and unphysical values for the wind work on the MKE and EKE reservoirs have to be balanced by other terms. These terms turn out to be the MKE to MPE conversion (black thick arrow, Figure 8(a)), and further the baroclinic instability pathway (red arrows, Figure 8(a)), because in the KE energy budget (equation (6)) the surface vertical

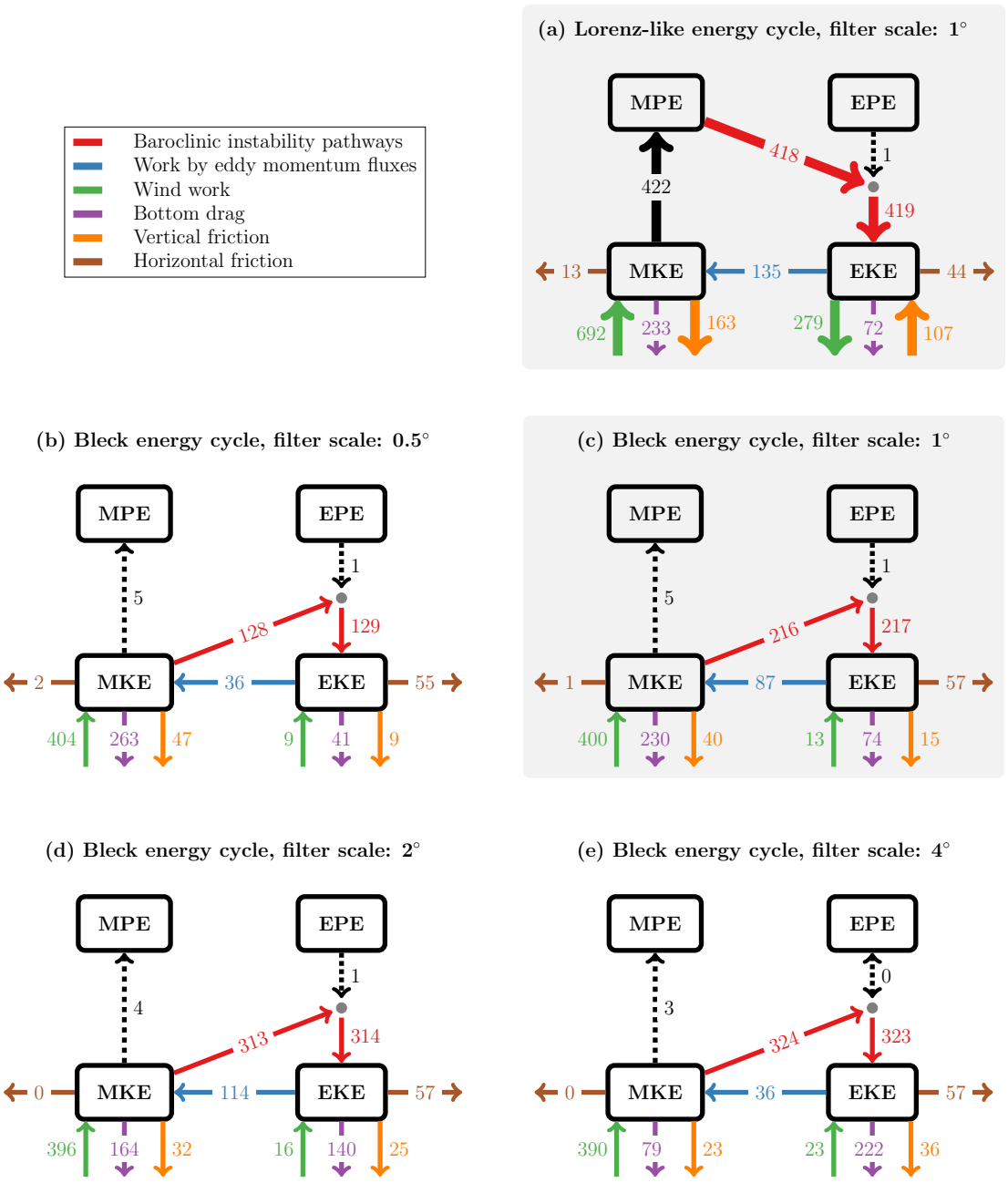

FIG. 8. (a) Lorenz-like and (b)-(e) Bleck energy diagrams (cf. Figure 3) diagnosed in the NeverWorld2 simulation for varying filter scales. The values show the domain-integrated energy conversion terms, averaged over 500 days, in units of GW. Here, we converted the domain integrals from $m^5\ s^{-3}$ to GW = 10^9 kg $m^2\ s^{-3}$ using NeverWorld2's reference density of 1000 kg m^{-3}. The thick arrows in (a) indicate energy conversion terms that have unphysical (too large) values, due to applying isopycnal non-thickness-weighted averaging. The cycles with gray background are for a filter scale of 1°, and thus summarize the cycles discussed in section 3.

stresses, $h_n \boldsymbol{u}_n \cdot \boldsymbol{F}_n^v$, are largely balanced by $-h_n \boldsymbol{u}_n \cdot \nabla M_n$ KE to PE.

(not shown); the latter term quantifies conversion from

The Bleck diagram (Figure 8(c)) is the natural choice when studying the energy cycle in isopycnal coordinates, and reliably characterizes the NeverWorld2 energetics. 230/(400+87) = 47% of the energy that enters the MKE reservoir via wind work and KE backscatter leaves the MKE reservoir via bottom drag, while 216/(400+87) = 44% of the energy gets routed to the EKE reservoir via baroclinic conversion. 87/217 = 40% of the energy that arrives at the EKE reservoir by baroclinic conversion gets transferred back to the mean flow, while the remaining fraction gets dissipated by bottom drag and horizontal friction.

The numbers reported in the previous paragraph hold for a filter scale of 1° and in a domain-integrated sense. As the filter scale is varied, the magnitude and relative importance of the energy conversion terms change (Figures 8(b)-(e)). Moreover, Figures 4, 6 and 7 reveal that the energy conversion terms have strong spatial variations. In the next section, we will investigate the energy cycles in Figures 8(b)-(e) more closely, both as a function of space and filter scale.

4. Energy cycle as a function of scale

In this section, we explore the energy cycle as a function of scale by applying different filter scales: 0.5°, 1°, 2°, and 4°. Figure 9 attempts to put our four filter scales into context with NeverWorld2's KE spectra and characteristic length scales: the energy-containing scale (black solid vertical line) and the first deformation scale (black dotted vertical line). The four colored wavenumber ranges are estimates for where the four filter scales fit into the spectrum. Each of the four filter scales is represented as an entire range of wavenumbers because the corresponding filter is anisotropic with different scales in zonal and meridional direction; a degree in longitude is smaller than a degree in latitude. We acknowledge that there is additional ambiguity about how to assign a wavenumber to each filter scale because our Gaussian filter is not "sharp", i.e., it does not cleanly separate scales below and above the filter scale (Grooms et al. 2021). Finally, we note that in Figure 9, we associate the filter scale with only half of a wavelength (via $k_L = \pi/L$), because our Gaussian filter has a length scale qualitatively similar to a boxcar filter whose width (not radius) is equal to the filter scale (Grooms et al. 2021).

In the following, we only consider the TWA Bleck cycle due to the deficiency of the non-TWA Lorenz-like cycle that was discussed in the previous section. We further focus on the energy pathways that affect the EKE budget. Figures 10 and 11 show the zonally and meridionally integrated EKE budget for the four filter scales, where the meridional integral in Figure 11 only spans the latitudes of the circumpolar channel. In both figures, the terms are

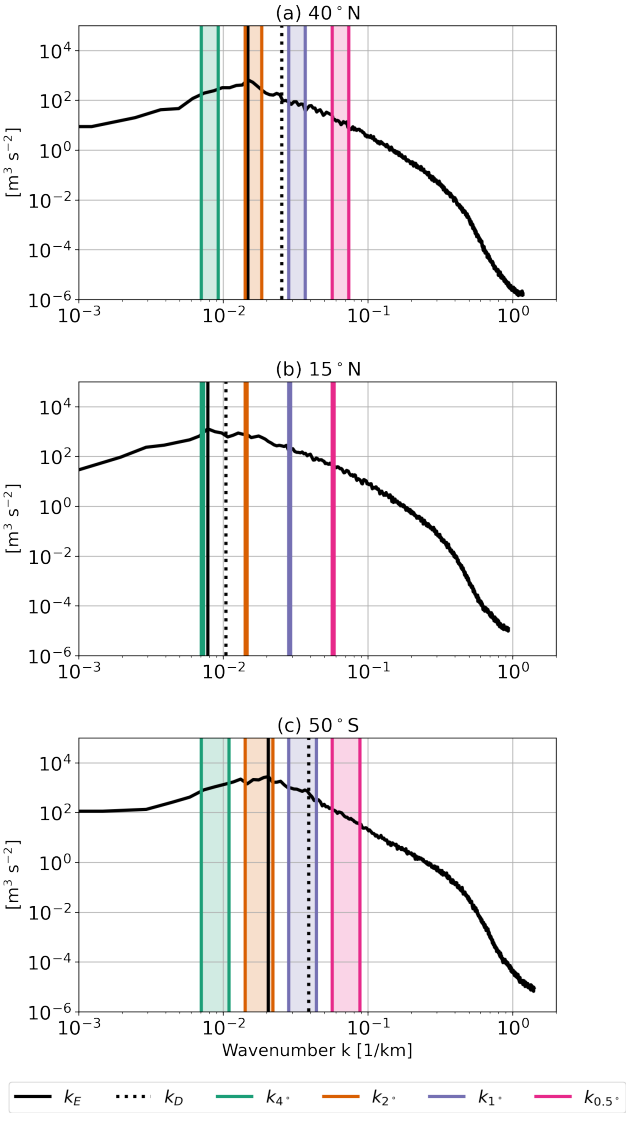

FIG. 9. 500-day averaged surface kinetic energy spectra at three latitudes: (a) 40°N, (b) 15°N, and (c) 50°S. The spectra are computed with the Python package `xrft` (Uchida et al. 2021) from the surface meridional eddy velocity fields defined as deviations from a 500-day averaged meridional velocity. Linear detrending and a Hann smoothing window are applied. In each panel, the vertical black solid line marks the wavenumber k_E at which the spectrum peaks, corresponding to the energy-containing scale. The dotted vertical line shows the deformation wavenumber $k_D = 1/L_D$ with zonally averaged first baroclinic deformation radius $L_D = c_1/\sqrt{f^2 + 2\beta c_1}$ (Hallberg 2013), where c_1 denotes the first-mode internal gravity wave speed, f the Coriolis parameter, and $\beta = \partial_y f$ its meridional gradient. The four colored wavenumber ranges are estimates for where our four filter scales fit into the spectrum. The low and high wavenumber ends of the ranges are given by $k_{Ly} = \pi/L_y$ and $k_{Lx} = \pi/L_x$, respectively, where $L_{x,y} = 4°, 2°, 1°, 0.5°$. Note that a degree in longitude is smaller than a degree in latitude, particularly at high latitudes, i.e., in (a) and (c).

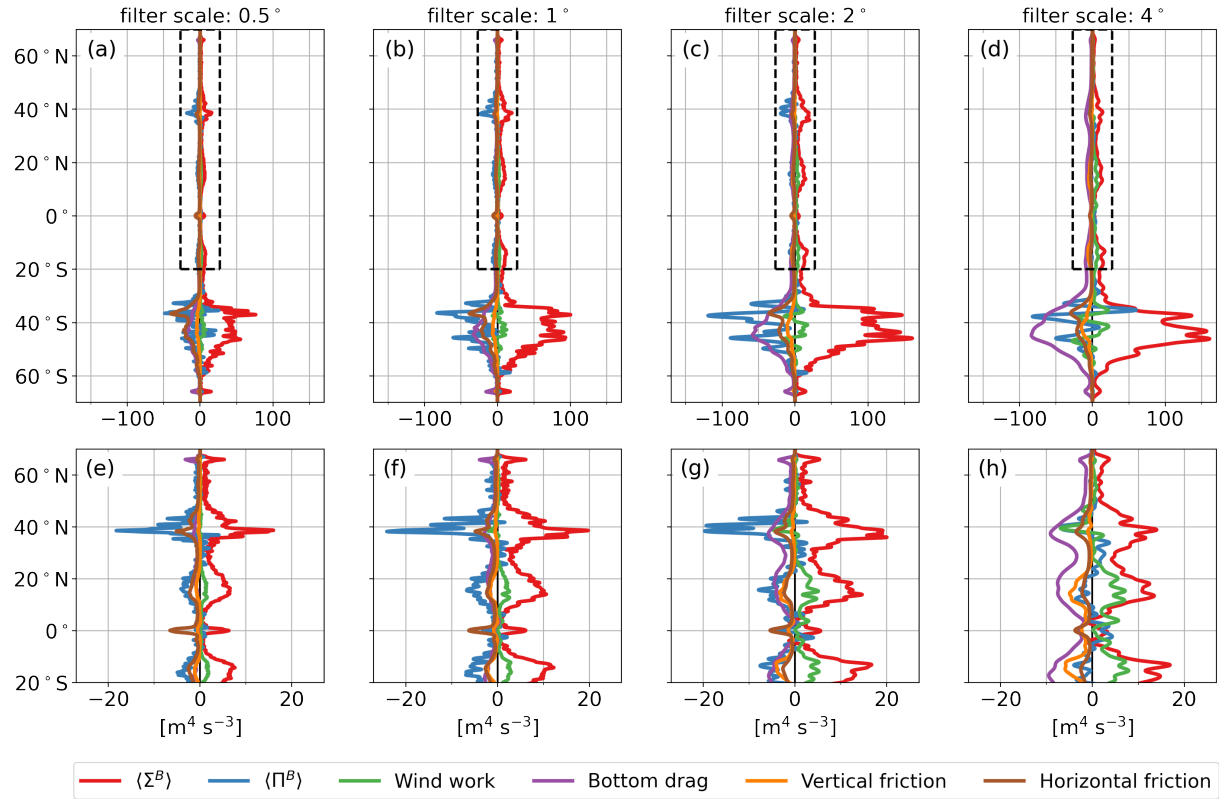

FIG. 10. EKE budget in the TWA framework for filter scales of (a),(e) 0.5°, (b),(f) 1°, (c),(g) 2°, (d),(h) 4°. All EKE budget terms are zonally integrated and averaged over 500 days. Panels (e)-(h) zoom in on the latitudes north of 20°S, marked by the dashed boxes in panels (a)-(d).

averaged over 500 days as before.

The EKE production by baroclinic instability, Σ^B (red line), increases steadily as we increase the filter scale from 0.5° to 4° but seems to have approximately saturated at 2° (Figures 8(b)-(e), 10, 11). These results suggest that baroclinic instability creates EKE over a range of scales, from below 0.5° to around 2°, since Σ^B integrates EKE production over all scales below the filter scale. The scale range bounded by 0.5° and 2° (pink, purple, and orange ranges) encompasses the first deformation scale at high latitudes (Figures 9(a),(c)) but falls below the first deformation scale at low latitudes (Figure 9(b)).

Next, we examine the behavior of the work done by eddy momentum fluxes, Π^B, for varying filter scale. At fixed latitude, the amplitude of $-\Pi^B$ (blue line) grows as the filter scale is increased from 0.5° to 1°, stays approximately constant across filter scales of 1° and 2°, and drops to values close to zero as the filter scale is further increased to 4° (Figures 8(b)-(e), Figure 10). These results suggest a KE inverse cascade on scales from below 0.5° to around 2°, with a peak between 1° and 2°. The 2° scale marks approximately the energy-containing scale at high latitudes (Figures 9(a),(c)). The significant negative values for Π^B at the 0.5° scale (Figure 10(e)) imply that the small-scale end (or start) of the inverse cascade lies well below the first deformation scale in our entire domain (pink range vs. dotted line, Figures 9(a)-(c)).

In the previous paragraph, we have discussed Π^B in a zonally integrated picture. Figure 11 provides a more detailed view of Π^B as a function of longitude in the channel, where Π^B is sign-indefinite. Positive values for Π^B are found downstream of Scotia Arc, near 10°E, and downstream of the mid-Atlantic ridge, near 40°E and 45°E, as already seen in Figure 7. Note that in Figure 11, it is difficult to identify the exact lag between the peaks of the Scotia Arc topography and Π^B, due to the semi-circular geometry of Scotia Arc (solid vs. dotted lines, Figure 11(e)). The positive values for Π^B downstream of topography indicate that the downscale energy transfer created by barotropic instability outpaces an KE inverse cascade. With increasing filter scale, the downscale energy transfer by barotropic instability becomes larger (Figure 11(a)-(d)). Downstream of locations with barotropic instability (positive Π^B), there is a strong upscale KE transfer (negative Π^B), consistent with the Π^B dipoles that we observed in Figure 7.

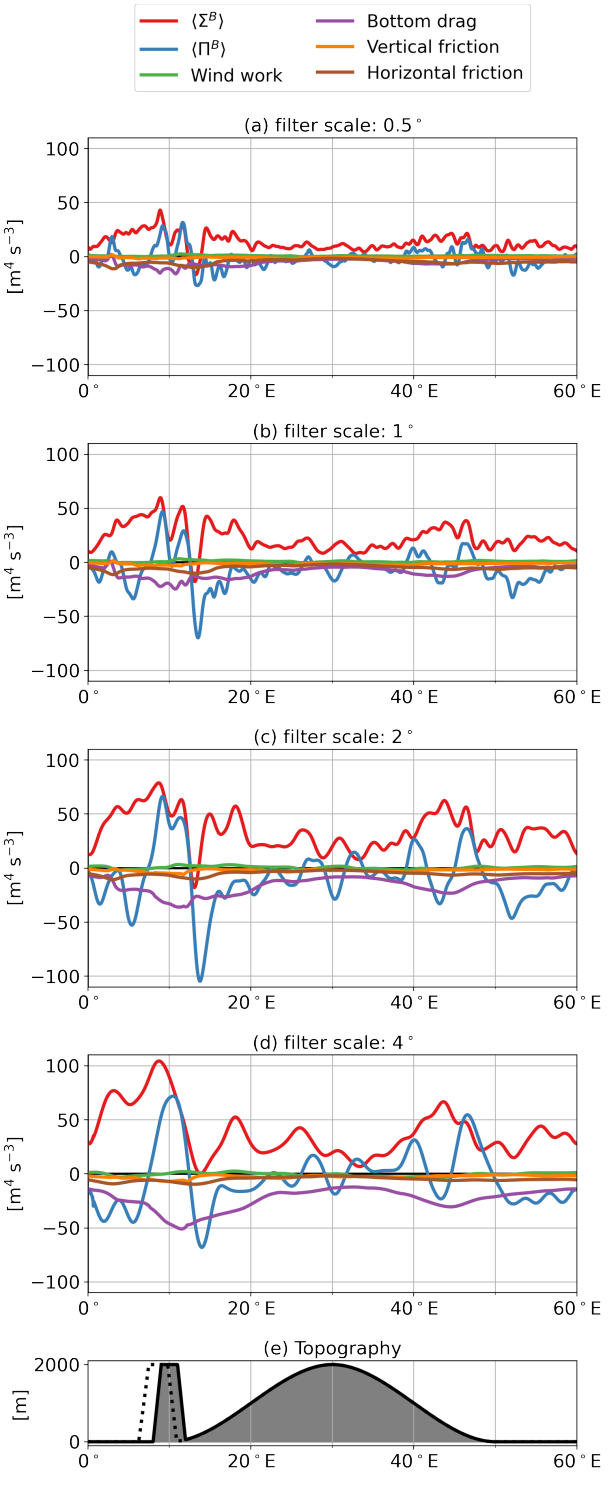

FIG. 11. (a)-(d) As Figure 10, but now the EKE budget terms are integrated meridionally (rather than zonally). The meridional integral spans the latitudes of the circumpolar channel, from 60°S to 40°S. (e) Topography along the latitude bands of 50°S (solid line and shading) and 45°S (dotted line).

Figure 12 shows the ratio of the zonal integrals of Π^B and Σ^B for our four filter scales. Here, we have applied a running mean with a latitude window of 10°, which smooths out strong latitudinal fluctuations in the "raw" values of the computed ratio. In the following, we will only discuss the smoothed values (blue thick lines rather than thin lines). A value of -1 indicates that 100% of the energy that is routed to the EKE reservoir via baroclinic conversion gets backscattered to the mean flow by eddy momentum fluxes (in a zonally integrated sense). A value of +1 implies mixed instability, with barolinic and barotropic instability being of the same amplitude (again in a zonally integrated sense).

Figure 12 highlights that the ratio of Π^B to Σ^B has much stronger dependence on the latitude and dynamical regime than on the filter scale, if one considers only the three smallest filter scales (Figures 12(a)-(c)). The regions of strongest relative backscatter, $-\Pi^B/\Sigma^B$, are marked by the latitude bands shaded in gray. In the Gulf stream region (centered at 40°N) 70-80% of the energy gets backscattered, in the subtropical return flows (centered at ±15°N) relative backscatter measures 40-60%, and in the recirculation region (centered at 35°S) we find relative backscatter of 70-100%. For a filter scale of 4°, the ratio Π^B/Σ^B is generally small in amplitude consistent with our previous finding that at this filter scale the EKE production Σ^B is peaked while the work of eddy momentum fluxes Π^B is minimal (Figures 8(b)-(e)). In a globally integrated sense, we find relative backscatter of 28%, 40%, 36%, and 11% for filter scales of 0.5°, 1°, 2°, and 4° (Figures 8(b)-(e)).

In the channel between 40°S and 60°S, we observe relative backscatter of up to 40% (Figure 12). We note, however, that the values between 40°S and 60°S have to be treated with care because the zonally integrated metrics in Figure 12 blur the topography-induced longitudinal dependence of Σ^B and Π^B. Indeed, comparing Π^B and Σ^B (blue vs. red lines) in Figure 11 reveals that relative backscatter can take values larger than 100% near 15°E. As discussed before, these are the locations where Σ^B and Π^B are likely to be spatially decoupled; the strong upscale energy transfer (negative Π^B of large amplitude) is partially fed by EKE transported from upstream regions.

Relative backscatter of less than 100% in the majority of the domain means that EKE gets extracted via other energy pathways: dissipation by bottom drag, vertical, and horizontal friction (Figures 8(b)-(e), 10, 11). Bottom drag is the dominant EKE sink; it increases with filter scale because increasing the filter scale makes the EKE reservoir larger. The amount of EKE dissipation by horizontal friction stays constant when varying the filter scale, a consequence of horizontal friction occurring only at the smallest

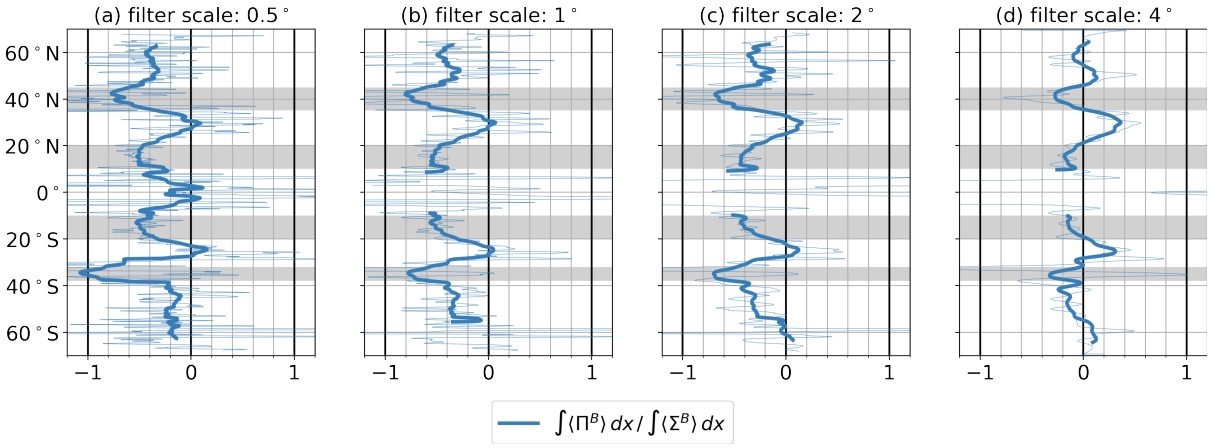

FIG. 12. Ratio of the zonal integrals of the work done by eddy momentum fluxes and EKE production, $\int\langle\Pi^B\rangle dx / \int\langle\Sigma^B\rangle dx$, as a function of latitude for filter scales of (a) 0.5°, (b) 1°, (c) 2°, and (d) 4°. All budget terms are averaged over 500 days. The thin lines show the values of the "raw" ratios, and the thick lines a running mean with a latitude window of 10°. The running mean smooths out strong fluctuations in latitudinal direction. The missing values are around latitudes where the zonal integral of Σ^B is smaller than 0.1 $m^4\ s^{-3}$ (cf. Figure 10). The latitude ranges shaded in gray identify the regions with strongest relative backscatter, i.e., most negative $\int\langle\Pi^B\rangle dx / \int\langle\Sigma^B\rangle dx$.

scales (smaller than our smallest filter scale of 0.5°). The amount of EKE dissipation by vertical friction increases with filter scale, which may be an artifact of bottom drag remnants improperly classified as vertical friction.

5. Summary and discussion

Incomplete knowledge of how energy is exchanged across scales has inhibited oceanographers from fully accounting for the ocean's energy budget, and adequately representing it in ocean models (Ferrari and Wunsch 2009). To gain better insights into the ocean energy cycle, we derived and investigated Lorenz-like and Bleck energy cycles in a high-resolution isopycnal model via isopycnal averaging. In contrast to most previous studies, we used a spatial filter rather than a temporal Reynolds average. This enabled us to map out the energy cycle in scale, space, and time, where we have focused on 500-day averaged budget terms in this study. Our scale-dependent energy cycles account for the non-commutativity of our filter with spatial derivatives, and are consistent with parameterization requirements of coarse-resolution climate simulations.

a. Lorenz versus Bleck cycle

Layer thickness and surface stresses in the top boundary layer are anticorrelated, no matter if the layered diagnostics originate from an isopycnal- or z-coordinate model. An along-isopycnal, non-thickness-weighted average (non-TWA) misses these anticorrelations, which leads to an unphysical decomposition of the energetic effects of vertical stresses into non-TWA mean and eddy contributions. The unphysical decomposition, in turn, leads to a misleading Lorenz-like energy diagram. This problem arises regardless of whether the non-TWA filter is spatial or temporal. We anticipate the deficiencies in the isopycnally averaged Lorenz-like energy cycle to become less pronounced if there are more (thus thinner) diagnosed model layers than the 15 used in NeverWorld2, but the problem will not be eliminated. We conclude that TWA provides *the* natural framework for isopycnal coordinates, and leads to a Bleck energy cycle with well characterized energy pathways.

We emphasize that the issues summarized in the previous paragraph are specific to isopycnally averaged data and that our results do not raise concerns about using the Eulerian-mean Lorenz energy cycle. In fact, the Eulerian-mean Lorenz energy cycle is expected to yield similar results to our isopycnally averaged Bleck cycle, even though the conversion terms associated with baroclinic instability appear in different places within the cycles.

b. Cross-scale energy transfers

Two energy pathways in the Bleck diagram are particularly interesting since they describe cross-scale energy transfers, between the mean flow and the eddies. The first one is the baroclinic instability pathway, which in the Bleck diagram converts MKE to eventually EKE (Σ^B). We found largest EKE production in the ACC-like channel. In all regions, EKE production occurs over a wide range of scales. At high latitudes, EKE production peaks near the first deformation scale, broadly consistent with 2-layer QG theory (Larichev and Held 1995; Held and Larichev 1996). At low latitudes, EKE production occurs on a wide range of scales that is entirely below the first deformation scale. The latter result is in agreement with the QG simulations in Roullet et al. (2012), who

show that in Charney-like regimes all scales below the first deformation scale are energized by baroclinic instability.

The second cross-scale energy transfer is the work done by eddy momentum fluxes (Π^B). In the following, we discuss the behavior and scale-dependence of Π^B; first in regions away from topography, and then in regions near topography.

1) Away from topography

Away from topography, Π^B is negative indicating a KE inverse cascade. The upscale KE transfer peaks near the energy-containing scale at high latitudes consistent with Schlösser and Eden (2007); Kjellsson and Zanna (2017), but below the deformation scale at low latitudes. Likewise, we find that the small-scale end (or start) of the inverse cascade lies well below the first deformation scale in all regions. Prior observational and modeling studies have suggested that at low latitudes the small-scale end of the inverse cascade is at scales smaller than the first deformation scale (e.g., Scott and Wang 2005; Schlösser and Eden 2007; Tulloch et al. 2011), consistent with our results. At high latitudes, however, these studies have found an ocean inverse cascade predominantly on scales larger than the deformation scale, in disagreement with our findings. Our results support the conclusions by Arbic et al. (2013) who analyze output from a realistic ocean model of 1/32° horizontal resolution (which matches the horizontal resolution of our simulation) and find a KE inverse cascade at scales smaller than the deformation scale at all latitudes (see their Figures 8-10). Arbic et al. (2013) also discuss the possibility that data of lower resolution may show a shifted inverse cascade biased to larger scales. The upcoming high-resolution data from wide-swath satellite altimeters (Fu et al. 2012) may shed more light on the scales involved in the KE cascade.

For regions where Π^B is negative (i.e., upscale), we define relative backscatter as the ratio between $-\Pi^B$ and Σ^B. Relative backscatter has strong sensitivity to the flow regime but relatively small scale sensitivity within the eddy-rich to eddy-permitting regime (which we hypothesize the filter scale range between 0.5° to 2° to be representitive of). In the eddy-permitting regime, relative backscatter measures 35-40% globally (Figures 8(c),(d)), but can take values up to 70-80% in western boundary jet regions (Figures 12(b),(c)).

2) Near topography

Interactions with topography can change the horizontal shear of ocean currents and make the mean flow unstable to barotropic instability, generating eddies through the work of eddy momentum fluxes. This is the picture that we observed in the ACC-like channel, where a strong flow interacts with topography. Regardless of the filter scale, Π^B is positive downstream of topography suggesting that barotropic instability transfers KE downscale from the mean flow to the eddies. With larger filter scales, the downscale energy transfer by barotropic instability increases.

After receiving KE from the mean flow through barotropic instability, the eddies transport KE downstream, where (part of) the KE is transferred back to the mean flow by eddy momentum fluxes. The upscale energy transfer in these downstream regions (-Π^B) can exceed the local EKE production (Σ^B), leading to a relative backscatter of more than 100%. This highlights that here Σ^B and Π^B are spatially decoupled and that the upscale energy transfer by eddy momentum fluxes is partially fed by EKE transported from upstream regions. The chain of events of topography-induced barotropic instability, followed by a downstream transport of EKE, and energy backscatter to the mean flow, is consistent with the results from idealized channel models in Youngs et al. (2017) and Barthel et al. (2017). The importance of EKE transport has been highlighted in idealized modeling studies (e.g., Grooms et al. 2013; Grooms 2017), but requires more detailed assessment in more complex models.

c. Caveats

Our energy cycles are diagnosed from a stacked shallow water model, which misses many processes that are present in the real ocean: surface buoyancy fluxes, a mixed layer, air-sea interactions, diabatic processes, and seasonal variations. For instance, Guo et al. (2022) show that air-sea interactions and diabatic mixing modify the energy cycle, and make baroclinic instability a less efficient mechanism for EKE generation. This modification would change the baroclinic instability pathway in our energy cycles (red arrows, Figure 3) as follows: Σ (transferring energy to the EKE reservoir) would be of smaller amplitude than Γ (originating in the MPE or MKE reservoirs), due to an alteration of the EPE budget.

Another aspect that has to be considered with caution is that the diagnosed energy cycle may be sensitive to the chosen horizontal eddy viscosity and viscosity scheme in models (Jochum et al. 2008; Arbic et al. 2013; Pearson et al. 2017). Further work is needed to assess how different horizontal viscosity formulations affect EKE dissipation, backscatter, and the entire energy cycle in ocean models, and how mesoscale eddy energy is dissipated in the real ocean (Wunsch and Ferrari 2004; Ferrari and Wunsch 2009).

d. Implications for mesoscale eddy parameterizations

Our diagnosed energy cycles lend themselves to evaluate the energetics of a wide range of mesoscale eddy parameterizations: schemes that mimic energy extraction by baroclinic instability from the mean flow (e.g., Gent and McWilliams 1990; Visbeck et al. 1997; Marshall et al. 2012; Greatbatch and Lamb 1990), Reynolds stress parameterizations (e.g., Zanna et al. 2017), and parameterizations that make use of an explicit eddy energy budget (Marshall and Adcroft 2010; Jansen et al. 2015; Eden and Greatbatch 2008). The evaluation of parameterizations via our diagnosed energy cycles is the objective of a follow-up paper, and we confine our discussion to only a few selected points in the following.

Bachman (2019) recently introduced the GM+E parameterization, which considers the total depth-integrated potential energy extracted by the GM (Gent and McWilliams 1990) scheme and re-injects it into the barotropic momentum via a negative harmonic viscosity. An open question is how to specify the energy throughput factor in the GM+E parameterization, which represents the fraction of energy transferred from GM to the Reynolds stress parameterization. Although the GM+E parameterization was not developed for the TWA framework, we hypothesize that our diagnostic $-\Pi^B/\Sigma^B$ may provide insights into how to choose the throughput factor. On the other hand, we found that relative backscatter depends on the flow regime in a complex manner, and that Σ^B and Π^B may be spatially decoupled near topography. This complexity advocates for employing a parameterized eddy energy equation (Eden and Greatbatch 2008; Jansen et al. 2019; Mak et al. 2018), in which EKE can be modulated by flow-dependent dissipation and EKE transport before being backscattered to the mean flow.

A final remark is that the *scale-dependence* of our diagnosed energy cycles provides a means of testing whether mesoscale eddy parameterizations scale correctly for different model resolutions. Developing scale- and flow-aware parameterizations is an ongoing research topic (e.g., Fox-Kemper and Menemenlis 2008; Bachman et al. 2017; Pearson et al. 2017), as we are entering the era of climate models in the 'gray-zone', where eddies are partially resolved in some but not all regions of the global ocean (Hallberg 2013). We hope that our diagnosed energy cycles provide a useful framework for evaluating and improving scale-aware mesoscale eddy parameterizations in ocean models.

Acknowledgments. We thank Gustavo Marques for running the NeverWorld2 simulations, and Hemant Khatri for help with implementing the thickness-weighted momentum and energy diagnostics. The analysis in this paper was greatly helped by the use of the `xarray` (Hoyer and Hamman 2017) and `xgcm` (Abernathey et al. 2022) Python packages. This work was generously funded by NSF grants OCE-1912332 (Loose, Grooms), OCE-1912420 (Bachman) and OCE-1912163 (Jansen) as part of the Ocean Transport and Eddy Energy Climate Process Team. We thank the entire team for insightful discussions. We would like to acknowledge high-performance computing support from Cheyenne (doi:10.5065/D6RX99HX) provided by NCAR's Computational and Information Systems Laboratory, sponsored by the National Science Foundation.

Data availability statement. Code that generates the figures in this paper is available at `https://github.com/NoraLoose/loose_bachman_grooms_jansen_2022_jpo`. As soon as the NeverWorld2 data is made available in the cloud, we will provide python-based jupyter notebooks at `https://github.com/NoraLoose/energy_cycles`, with which the computation of the Lorenz-like and Bleck energy cycles in this paper is fully reproducible.

APPENDIX

A1. Mean and eddy potential energy budgets

The budget for MPE is identical in the non-TWA and TWA frameworks, and the same holds true for the EPE budget. To obtain the MPE budget, we first filter the thickness equation (1) and depth-integrated PE equation (5), and obtain

$$\partial_t \bar{h}_n = -\overline{\nabla \cdot (h_n \boldsymbol{u}_n)}, \tag{A1}$$

$$\partial_t \overline{\left(\sum_{n=0}^{N-1} \mathrm{PE}_n \right)} = -\sum_{n=1}^{N} \overline{M_n \nabla \cdot (h_n \boldsymbol{u}_n)}. \tag{A2}$$

Using the definition of MPE (7) and the filtered thickness equation (A2), we perform a similar calculation as in equation (5) and obtain

$$\begin{aligned} \partial_t (\mathrm{MPE}) &= -\sum_{n=1}^{N} \bar{M}_n \overline{\nabla \cdot (h_n \boldsymbol{u}_n)} \\ &= -\nabla \cdot \left(\sum_{n=1}^{N} \overline{h_n \boldsymbol{u}_n} \bar{M}_n \right) + \sum_{n=1}^{N} \overline{h_n \boldsymbol{u}_n} \nabla \bar{M}_n + \mathcal{E}, \end{aligned} \tag{A3}$$

where

$$\mathcal{E} = \sum_{n=1}^{N} \left(\nabla \cdot (\overline{h_n \boldsymbol{u}_n}) - \overline{\nabla \cdot (h_n \boldsymbol{u}_n)} \right) \bar{M}_n \tag{A4}$$

is an extra term that arises because the filter does not commute with spatial derivatives. Note that the two last terms in equation (A3) appear as energy transfers

in and out of the MPE reservoir in Figures 3(a),(b), where Figure 3(b) uses identity (11). The first term in equation (A3) is a flux divergence that integrates to zero over the domain, and does not enter the energy conversion diagrams.

The EPE budget is obtained by subtracting the MPE budget (A3) from the filtered PE budget (A2):

$$\partial_t(\mathrm{EPE}) = -\sum_{n=1}^{N}\left(\overline{M_n\nabla\cdot(h_n\boldsymbol{u}_n)} - \bar{M}_n\overline{\nabla\cdot(h_n\boldsymbol{u}_n)}\right). \quad \text{(A5)}$$

A2. Mean and eddy kinetic energy budgets

We filter the KE budget (6), and obtain

$$\begin{aligned}\partial_t(\overline{\mathrm{KE}_n}) = &-\overline{\nabla\cdot(\boldsymbol{u}_n\mathrm{KE}_n)} - \overline{h_n\boldsymbol{u}_n\cdot\nabla M_n}\\ &+\overline{h_n\boldsymbol{u}_n\cdot\boldsymbol{F}_n^v} + \overline{h_n\boldsymbol{u}_n\cdot\boldsymbol{F}_n^h}. \end{aligned}\quad \text{(A6)}$$

The filtered KE budget will enter the EKE budgets in both the non-TWA and TWA frameworks.

a. Non-TWA Framework

First, we filter the velocity equation (2) and obtain

$$\partial_t\bar{\boldsymbol{u}}_n + \overline{\boldsymbol{u}_n\cdot\nabla\boldsymbol{u}_n} + \overline{\boldsymbol{f}\times\boldsymbol{u}_n} = -\overline{\nabla M_n} + \overline{\boldsymbol{F}_n^v} + \overline{\boldsymbol{F}_n^h}, \quad \text{(A7)}$$

where we denote $\boldsymbol{f} = f\hat{\boldsymbol{z}}$ and we have used the identity $\boldsymbol{u}_n\cdot\nabla\boldsymbol{u}_n = (\nabla\times\boldsymbol{u}_n)\times\boldsymbol{u}_n + \nabla K_n$. We obtain the MKE budget by multiplying the filtered thickness equation (A1) with $\frac{1}{2}|\bar{\boldsymbol{u}}_n|^2$, adding this to $\bar{h}_n\bar{\boldsymbol{u}}_n$ times the filtered velocity equation (A7), and summing over all layers:

$$\begin{aligned}\partial_t(\mathrm{MKE}) = &-\sum_{n=1}^{N}\nabla\cdot\left(\bar{\boldsymbol{u}}_n\frac{\bar{h}_n|\bar{\boldsymbol{u}}_n|^2}{2}\right) - \sum_{n=1}^{N}\bar{h}_n\bar{\boldsymbol{u}}_n\cdot\overline{\nabla M_n}\\ &-\Pi^L + \sum_{n=1}^{N}\bar{h}_n\bar{\boldsymbol{u}}_n\cdot\overline{\boldsymbol{F}_n^v} + \sum_{n=1}^{N}\bar{h}_n\bar{\boldsymbol{u}}_n\cdot\overline{\boldsymbol{F}_n^h}, \end{aligned}\quad \text{(A8)}$$

where

$$\begin{aligned}\Pi^L = &\sum_{n=1}^{N}\bar{h}_n\bar{\boldsymbol{u}}_n\cdot\overline{\boldsymbol{f}\times\boldsymbol{u}_n} + \sum_{n=1}^{N}\bar{h}_n\bar{\boldsymbol{u}}_n\cdot\left(\overline{\boldsymbol{u}_n\cdot\nabla\boldsymbol{u}_n} - \bar{\boldsymbol{u}}_n\cdot\nabla\bar{\boldsymbol{u}}_n\right)\\ &+\sum_{n=1}^{N}\frac{|\bar{\boldsymbol{u}}_n|^2}{2}\left(\overline{\nabla\cdot(h_n\boldsymbol{u}_n)} - \nabla\cdot(\bar{h}_n\bar{\boldsymbol{u}}_n)\right) \end{aligned}\quad \text{(A9)}$$

is the work done by eddy momentum fluxes. The first term on the right hand side of (A8) is the advection of MKE by the mean flow, which integrates to zero over the domain, and does not enter the energy conversion diagram. The remaining terms on the right hand side of (A8) appear as conversion terms starting from or ending in the MKE reservoir in Figure 3(a).

We obtain the EKE budget by subtracting the MKE budget (A8) from the filtered KE budget (A6):

$$\begin{aligned}\partial_t(\mathrm{EKE}) = &-\mathcal{T}^L + \Sigma^L + \Pi^L\\ &+\sum_{n=1}^{N}\left(\overline{h_n\boldsymbol{u}_n\cdot\boldsymbol{F}_n^v} - \bar{h}_n\bar{\boldsymbol{u}}_n\cdot\overline{\boldsymbol{F}_n^v}\right)\\ &+\sum_{n=1}^{N}\left(\overline{h_n\boldsymbol{u}_n\cdot\boldsymbol{F}_n^h} - \bar{h}_n\bar{\boldsymbol{u}}_n\cdot\overline{\boldsymbol{F}_n^h}\right)\end{aligned}$$

where

$$\mathcal{T}^L = \sum_{n=1}^{N}\left[\overline{\nabla\cdot(\boldsymbol{u}_n\mathrm{KE}_n)} - \nabla\cdot\left(\bar{\boldsymbol{u}}_n\frac{\bar{h}_n|\bar{\boldsymbol{u}}_n|^2}{2}\right)\right], \quad \text{(A10)}$$

$$\Sigma^L = -\sum_{n=1}^{N}\left(\overline{h_n\boldsymbol{u}_n\nabla M_n} - \bar{h}_n\bar{\boldsymbol{u}}_n\overline{\nabla M_n}\right) \quad \text{(A11)}$$

are the EKE transport and production terms, respectively. Note that

$$\begin{aligned}\Sigma^L = &\underbrace{-\sum_{n=1}^{N}\left(\overline{h_n\boldsymbol{u}_n}\nabla\bar{M}_n - \bar{h}_n\bar{\boldsymbol{u}}_n\overline{\nabla M_n}\right) - \mathcal{E}}_{\Gamma^L,\ \text{Figure 3(a)}}\\ &+\underbrace{\sum_{n=1}^{N}\left(\overline{M_n\nabla\cdot(h_n\boldsymbol{u}_n)} - \bar{M}_n\overline{\nabla\cdot(h_n\boldsymbol{u}_n)}\right)}_{-\partial_t\mathrm{EPE}} + \mathcal{D}, \end{aligned}\quad \text{(A12)}$$

where

$$\mathcal{D} = -\sum_{n=1}^{N}\left(\overline{\nabla\cdot(h_n\boldsymbol{u}_nM_n)} - \nabla\cdot(\overline{h_n\boldsymbol{u}_n}\bar{M}_n)\right). \quad \text{(A13)}$$

Identity (A12) shows that the three arrows that meet at the gray circle in Figure 3(a) only differ by the flux divergence $\mathcal{D}$, which integrates to zero over the domain.

b. TWA Framework

First, we derive a budget for the filtered thickness-multiplied velocity, $\overline{h_n\boldsymbol{u}_n}$. To this aim, we multiply the velocity equation (2) by h_n, the thickness equation (1) by $\boldsymbol{u}_n$, add the two, and filter:

$$\begin{aligned}\partial_t(\overline{h_n\boldsymbol{u}_n}) + \overline{h_n\boldsymbol{u}_n\cdot\nabla\boldsymbol{u}_n} + \overline{\boldsymbol{u}_n\nabla\cdot(h_n\boldsymbol{u}_n)} + \overline{\boldsymbol{f}\times h_n\boldsymbol{u}_n}\\ = -\overline{h_n\nabla M_n} + \overline{h_n\boldsymbol{F}_n^v} + \overline{h_n\boldsymbol{F}_n^h}.\end{aligned}\quad \text{(A14)}$$

The time derivative of MKE (equation (12)) in the TWA framework can be written as

$$\partial_t(\mathrm{MKE}) = \sum_{n=1}^{N}\left(\hat{\boldsymbol{u}}_n\partial_t(\overline{h_n\boldsymbol{u}_n}) - \frac{|\hat{\boldsymbol{u}}_n|^2}{2}\partial_t\bar{h}_n\right).$$

Using this identity together with equations (A1) and (A14), we obtain

$$\begin{aligned}\partial_t(\mathrm{MKE}) = &-\sum_{n=1}^{N}\nabla\cdot\left(\hat{\boldsymbol{u}}_n\frac{\bar{h}_n|\hat{\boldsymbol{u}}_n|^2}{2}\right) - \Pi^B\\ &-\sum_{n=1}^{N}\bar{h}_n\hat{\boldsymbol{u}}_n\cdot\nabla\bar{M}_n - \mathcal{E}\\ &+\sum_{n=1}^{N}\bar{h}_n\hat{\boldsymbol{u}}_n\cdot\left(\nabla\bar{M}_n - \widehat{\nabla M_n}\right) + \mathcal{E}\\ &+\sum_{n=1}^{N}\hat{\boldsymbol{u}}_n\cdot\overline{h_n\boldsymbol{F}_n^v} + \sum_{n=1}^{N}\hat{\boldsymbol{u}}_n\cdot\overline{h_n\boldsymbol{F}_n^h},\end{aligned} \tag{A15}$$

where

$$\begin{aligned}\Pi^B = &\sum_{n=1}^{N}\hat{\boldsymbol{u}}_n\cdot\overline{\boldsymbol{f}\times h_n\boldsymbol{u}_n}\\ &+\sum_{n=1}^{N}\hat{\boldsymbol{u}}_n\cdot\left(\overline{h_n\boldsymbol{u}_n\cdot\nabla\boldsymbol{u}_n} + \overline{\boldsymbol{u}_n\nabla\cdot(h_n\boldsymbol{u}_n)}\right.\\ &\left.-\bar{h}_n\hat{\boldsymbol{u}}_n\cdot\nabla\hat{\boldsymbol{u}}_n - \frac{\hat{\boldsymbol{u}}_n}{2}\left[\nabla\cdot(\bar{h}_n\hat{\boldsymbol{u}}_n) + \overline{\nabla\cdot(h_n\boldsymbol{u}_n)}\right]\right)\end{aligned} \tag{A16}$$

is the work done by eddy momentum fluxes. The first term on the right hand side of (A15) is the advection of MKE by the mean flow, which integrates to zero over the domain, and does not enter the energy conversion diagram. The remaining terms on the right hand side of (A15) appear as conversion terms starting from or ending in the MKE reservoir in Figure 3(b).

We obtain the TWA EKE budget by subtracting the MKE budget (A15) from the filtered KE budget (A6):

$$\begin{aligned}\partial_t(\mathrm{EKE}) = &-\mathcal{T}^B + \Sigma^B + \Pi^B\\ &+\sum_{n=1}^{N}\left(\overline{h_n\boldsymbol{u}_n\cdot\boldsymbol{F}_n^v} - \hat{\boldsymbol{u}}_n\cdot\overline{h_n\boldsymbol{F}_n^v}\right)\\ &+\sum_{n=1}^{N}\left(\overline{h_n\boldsymbol{u}_n\cdot\boldsymbol{F}_n^h} - \hat{\boldsymbol{u}}_n\cdot\overline{h_n\boldsymbol{F}_n^h}\right)\end{aligned}$$

where

$$\mathcal{T}^B = \sum_{n=1}^{N}\left[\overline{\nabla\cdot(\boldsymbol{u}_n\mathrm{KE}_n)} - \nabla\cdot\left(\hat{\boldsymbol{u}}_n\frac{\bar{h}_n|\hat{\boldsymbol{u}}_n|^2}{2}\right)\right], \tag{A17}$$

$$\Sigma^B = -\sum_{n=1}^{N}\left(\overline{h_n\boldsymbol{u}_n\nabla M_n} - \bar{h}_n\hat{\boldsymbol{u}}_n\widehat{\nabla M_n}\right) \tag{A18}$$

are the EKE transport and production terms, respectively. Note that

$$\begin{aligned}\Sigma^B = &\underbrace{-\sum_{n=1}^{N}\bar{h}_n\hat{\boldsymbol{u}}_n\cdot\left(\nabla\bar{M}_n - \widehat{\nabla M_n}\right) - \mathcal{E}}_{\Gamma^B,\ \text{Figure 3(b)}}\\ &+\underbrace{\sum_{n=1}^{N}\left(\overline{M_n\nabla\cdot(h_n\boldsymbol{u}_n)} - \bar{M}_n\overline{\nabla\cdot(h_n\boldsymbol{u}_n)}\right)}_{-\partial_t\mathrm{EPE}} + \mathcal{D},\end{aligned} \tag{A19}$$

in analogy to identity (A12).

References

Abernathey, R., and Coauthors, 2022: xgcm/xgcm: v0.6.2rc1. Zenodo, URL https://doi.org/10.5281/zenodo.6097129, https://doi.org/10.5281/zenodo.6097129.

Aiki, H., and K. J. Richards, 2008: Energetics of the Global Ocean: The Role of Layer-Thickness Form Drag. *Journal of Physical Oceanography*, **38 (9)**, 1845–1869, https://doi.org/10.1175/2008JPO3820.1.

Aiki, H., X. Zhai, and R. J. Greatbatch, 2015: Energetics of the global ocean: the role of mesoscale eddies. *Indo-Pacific Climate Variability and Predictability*, World Scientific Series on Asia-Pacific Weather and Climate, Vol. Volume 7, WORLD SCIENTIFIC, 109–134, https://doi.org/10.1142/9789814696623_0004.

Ajayi, A., J. L. Sommer, E. P. Chassignet, J.-M. Molines, X. Xu, A. Albert, and W. Dewar, 2021: Diagnosing Cross-Scale Kinetic Energy Exchanges From Two Submesoscale Permitting Ocean Models. *Journal of Advances in Modeling Earth Systems*, **13 (6)**, e2019MS001 923, https://doi.org/10.1029/2019MS001923.

Aluie, H., 2013: Scale decomposition in compressible turbulence. *Physica D: Nonlinear Phenomena*, **247 (1)**, 54–65, https://doi.org/10.1016/j.physd.2012.12.009.

Aluie, H., M. Hecht, and G. K. Vallis, 2018: Mapping the Energy Cascade in the North Atlantic Ocean: The Coarse-Graining Approach. *Journal of Physical Oceanography*, **48 (2)**, 225–244, https://doi.org/10.1175/JPO-D-17-0100.1.

Arbic, B. K., K. L. Polzin, R. B. Scott, J. G. Richman, and J. F. Shriver, 2013: On Eddy Viscosity, Energy Cascades, and the Horizontal Resolution of Gridded Satellite Altimeter Products. *Journal of Physical Oceanography*, **43 (2)**, 283–300, https://doi.org/10.1175/JPO-D-11-0240.1.

Bachman, S. D., 2019: The GME closure: A framework for coupling backscatter with the Gent and McWilliams parameterization. *Ocean Modelling*, **136**, 85–106, https://doi.org/10.1016/j.ocemod.2019.02.006.

Bachman, S. D., B. Fox-Kemper, and B. Pearson, 2017: A scale-aware subgrid model for quasi-geostrophic turbulence. *Journal of Geophysical Research: Oceans*, **122 (2)**, 1529–1554, https://doi.org/https://doi.org/10.1002/2016JC012265.

Barthel, A., A. M. Hogg, S. Waterman, and S. Keating, 2017: Jet–Topography Interactions Affect Energy Pathways to the Deep Southern Ocean. *Journal of Physical Oceanography*, **47 (7)**, 1799–1816, https://doi.org/10.1175/JPO-D-16-0220.1.

Bleck, R., 1985: On the conversion between mean and eddy components of potential and kinetic energy in isentropic and isopycnic coordinates. *Dynamics of Atmospheres and Oceans*, **9 (1)**, 17–37, https://doi.org/10.1016/0377-0265(85)90014-4.

Charney, J. G., 1947: THE DYNAMICS OF LONG WAVES IN A BAROCLINIC WESTERLY CURRENT. *Journal of the Atmospheric Sciences*, **4 (5)**, 136–162, https://doi.org/10.1175/1520-0469(1947)004<0136:TDOLWI>2.0.CO;2.

Chen, R., G. R. Flierl, and C. Wunsch, 2014: A Description of Local and Nonlocal Eddy–Mean Flow Interaction in a Global Eddy-Permitting State Estimate. *Journal of Physical Oceanography*, **44 (9)**, 2336–2352, https://doi.org/10.1175/JPO-D-14-0009.1.

Duhaut, T. H., and D. N. Straub, 2006: Wind stress dependence on ocean surface velocity: Implications for mechanical energy input to ocean circulation. *Journal of Physical Oceanography*, **36 (2)**, 202–211.

Eady, E. T., 1949: Long Waves and Cyclone Waves. *Tellus*, **1 (3)**, 33–52, https://doi.org/10.1111/j.2153-3490.1949.tb01265.x, _eprint: https://onlinelibrary.wiley.com/doi/pdf/10.1111/j.2153-3490.1949.tb01265.x.

Eden, C., and R. J. Greatbatch, 2008: Towards a mesoscale eddy closure. *Ocean Modelling*, **20 (3)**, 223–239, https://doi.org/10.1016/j.ocemod.2007.09.002.

Ferrari, R., and C. Wunsch, 2009: Ocean Circulation Kinetic Energy: Reservoirs, Sources, and Sinks. *Annual Review of Fluid Mechanics*, **41 (1)**, 253–282, https://doi.org/10.1146/annurev.fluid.40.111406.102139.

Fox-Kemper, B., and D. Menemenlis, 2008: Can Large Eddy Simulation Techniques Improve Mesoscale Rich Ocean Models? *Ocean Modeling in an Eddying Regime*, American Geophysical Union (AGU), 319–337, https://doi.org/10.1029/177GM19.

Fu, L.-L., D. Alsdorf, R. Morrow, E. Rodriguez, and N. Mognard, 2012: SWOT : the Surface Water and Ocean Topography Mission : wide-swath altimetric elevation on Earth. Technical Report, Pasadena, CA : Jet Propulsion Laboratory, National Aeronautics and Space Administration, 2012. URL https://trs.jpl.nasa.gov/handle/2014/41996, accepted: 2012-03-13T18:41:44Z.

Gent, P. R., and J. C. McWilliams, 1990: Isopycnal Mixing in Ocean Circulation Models. *Journal of Physical Oceanography*, **20 (1)**, 150–155, https://doi.org/10.1175/1520-0485(1990)020<0150:IMIOCM>2.0.CO;2.

Gill, A. E., J. S. A. Green, and A. J. Simmons, 1974: Energy partition in the large-scale ocean circulation and the production of mid-ocean eddies. *Deep Sea Research and Oceanographic Abstracts*, **21 (7)**, 499–528, https://doi.org/10.1016/0011-7471(74)90010-2.

Greatbatch, R. J., and K. G. Lamb, 1990: On Parameterizing Vertical Mixing of Momentum in Non-eddy Resolving Ocean Models. *Journal of Physical Oceanography*, **20 (10)**, 1634–1637, https://doi.org/10.1175/1520-0485(1990)020<1634:OPVMOM>2.0.CO;2.

Griffies, S. M., and R. W. Hallberg, 2000: Biharmonic Friction with a Smagorinsky-Like Viscosity for Use in Large-Scale Eddy-Permitting Ocean Models. *Monthly Weather Review*, **128 (8)**, 2935–2946, https://doi.org/10.1175/1520-0493(2000)128<2935:BFWASL>2.0.CO;2.

Grooms, I., 2017: Simulations of eddy kinetic energy transport in barotropic turbulence. *Physical Review Fluids*, **2 (11)**, 113 801, https://doi.org/10.1103/PhysRevFluids.2.113801.

Grooms, I., N. Loose, R. Abernathey, J. M. Steinberg, S. D. Bachman, G. Marques, A. P. Guillaumin, and E. Yankovsky, 2021: Diffusion-Based Smoothers for Spatial Filtering of Gridded Geophysical Data. *Journal of Advances in Modeling Earth Systems*, **13 (9)**, e2021MS002 552, https://doi.org/10.1029/2021MS002552.

Grooms, I., L.-P. Nadeau, and K. S. Smith, 2013: Mesoscale eddy energy locality in an idealized ocean model. *Journal of physical oceanography*, **43 (9)**, 1911–1923.

Gula, J., M. J. Molemaker, and J. C. McWilliams, 2016: Topographic generation of submesoscale centrifugal instability and energy dissipation. *Nature Communications*, **7 (1)**, 12 811, https://doi.org/10.1038/ncomms12811.

Guo, Y., S. Bishop, F. Bryan, and S. Bachman, 2022: A global diagnosis of eddy potential energy budget in an eddy permitting ocean model. *submitted*.

Hallberg, R., 2013: Using a resolution function to regulate parameterizations of oceanic mesoscale eddy effects. *Ocean Modelling*, **72**, 92–103, https://doi.org/10.1016/j.ocemod.2013.08.007.

Held, I. M., and V. D. Larichev, 1996: A Scaling Theory for Horizontally Homogeneous, Baroclinically Unstable Flow on a Beta Plane. *Journal of the Atmospheric Sciences*, **53 (7)**, 946–952, https://doi.org/10.1175/1520-0469(1996)053<0946:ASTFHH>2.0.CO;2.

Hoyer, S., and J. Hamman, 2017: xarray: N-D labeled Arrays and Datasets in Python. *Journal of Open Research Software*, **5 (1)**, 10, https://doi.org/10.5334/jors.148, URL http://openresearchsoftware.metajnl.com/articles/10.5334/jors.148/.

Jansen, M. F., A. Adcroft, S. Khani, and H. Kong, 2019: Toward an Energetically Consistent, Resolution Aware Parameterization of Ocean Mesoscale Eddies. *Journal of Advances in Modeling Earth Systems*, **11 (8)**, 2844–2860, https://doi.org/10.1029/2019MS001750.

Jansen, M. F., A. J. Adcroft, R. Hallberg, and I. M. Held, 2015: Parameterization of eddy fluxes based on a mesoscale energy budget. *Ocean Modelling*, **92**, 28–41, https://doi.org/10.1016/j.ocemod.2015.05.007.

Jochum, M., G. Danabasoglu, M. Holland, Y.-O. Kwon, and W. G. Large, 2008: Ocean viscosity and climate. *Journal of Geophysical Research: Oceans*, **113 (C6)**, https://doi.org/10.1029/2007JC004515.

Kang, D., and E. N. Curchitser, 2015: Energetics of Eddy–Mean Flow Interactions in the Gulf Stream Region. *Journal of Physical Oceanography*, **45 (4)**, 1103–1120, https://doi.org/10.1175/JPO-D-14-0200.1.

Kent, J., J. P. Whitehead, C. Jablonowski, and R. B. Rood, 2014: Determining the effective resolution of advection schemes. Part I: Dispersion analysis. *Journal of Computational Physics*, **278**, 485–496, https://doi.org/10.1016/j.jcp.2014.01.043.

Kjellsson, J., and L. Zanna, 2017: The Impact of Horizontal Resolution on Energy Transfers in Global Ocean Models. *Fluids*, **2 (3)**, 45, https://doi.org/10.3390/fluids2030045.

Larichev, V. D., and I. M. Held, 1995: Eddy Amplitudes and Fluxes in a Homogeneous Model of Fully Developed Baroclinic Instability. *Journal of Physical Oceanography*, **25 (10)**, 2285–2297, https://doi.org/10.1175/1520-0485(1995)025<2285:EAAFIA>2.0.CO;2.

Loose, N., and Coauthors, 2022: Gcm-filters: A python package for diffusion-based spatial filtering of gridded data. *Journal of Open Source Software*, **7 (70)**, 3947, https://doi.org/10.21105/joss.03947, URL https://doi.org/10.21105/joss.03947.

Lorenz, E. N., 1955: Available Potential Energy and the Maintenance of the General Circulation. *Tellus*, **7 (2)**, 157–167, https://doi.org/10.1111/j.2153-3490.1955.tb01148.x.

Mak, J., J. R. Maddison, D. P. Marshall, and D. R. Munday, 2018: Implementation of a Geometrically Informed and Energetically Constrained Mesoscale Eddy Parameterization in an Ocean Circulation Model. *Journal of Physical Oceanography*, **48 (10)**, 2363–2382, https://doi.org/10.1175/JPO-D-18-0017.1.

Marques, G., and Coauthors, 2022: Neverworld2: An idealized model hierarchy to investigate ocean mesoscale eddies across resolutions. *Earth and Space Science Open Archive*, 12, https://doi.org/10.1002/essoar.10511043.1, URL https://doi.org/10.1002/essoar.10511043.1.

Marshall, D. P., and A. J. Adcroft, 2010: Parameterization of ocean eddies: Potential vorticity mixing, energetics and Arnold's first stability theorem. *Ocean Modelling*, **32 (3)**, 188–204, https://doi.org/10.1016/j.ocemod.2010.02.001.

Marshall, D. P., J. R. Maddison, and P. S. Berloff, 2012: A Framework for Parameterizing Eddy Potential Vorticity Fluxes. *Journal of Physical Oceanography*, **42 (4)**, 539–557, https://doi.org/10.1175/JPO-D-11-048.1.

Molemaker, M. J., J. C. Mcwilliams, and X. Capet, 2010: Balanced and unbalanced routes to dissipation in an equilibrated Eady flow. *Journal of Fluid Mechanics*, **654**, 35–63, https://doi.org/10.1017/S0022112009993272.

Pearson, B., B. Fox-Kemper, S. Bachman, and F. Bryan, 2017: Evaluation of scale-aware subgrid mesoscale eddy models in a global eddy-rich model. *Ocean Modelling*, **115**, 42–58, https://doi.org/10.1016/j.ocemod.2017.05.007.

Plumb, R. A., 1983: A New Look at the Energy Cycle. *Journal of Atmospheric Sciences*, **40 (7)**, 1669–1688, https://doi.org/10.1175/1520-0469(1983)040<1669:ANLATE>2.0.CO;2.

Rai, S., M. Hecht, M. Maltrud, and H. Aluie, 2021: Scale of oceanic eddy killing by wind from global satellite observations. *Science Advances*, **7 (28)**, eabf4920, https://doi.org/10.1126/sciadv.abf4920.

Renault, L., M. J. Molemaker, J. C. McWilliams, A. F. Shchepetkin, F. Lemarié, D. Chelton, S. Illig, and A. Hall, 2016: Modulation of Wind Work by Oceanic Current Interaction with the Atmosphere. *Journal of Physical Oceanography*, **46 (6)**, 1685–1704, https://doi.org/10.1175/JPO-D-15-0232.1.

Roullet, G., J. C. McWilliams, X. Capet, and M. J. Molemaker, 2012: Properties of Steady Geostrophic Turbulence with Isopycnal Outcropping. *Journal of Physical Oceanography*, **42 (1)**, 18–38, https://doi.org/10.1175/JPO-D-11-09.1.

Schlösser, F., and C. Eden, 2007: Diagnosing the energy cascade in a model of the North Atlantic. *Geophysical Research Letters*, **34 (2)**, https://doi.org/10.1029/2006GL027813.

Scott, R. B., and F. Wang, 2005: Direct Evidence of an Oceanic Inverse Kinetic Energy Cascade from Satellite Altimetry. *Journal of Physical Oceanography*, **35 (9)**, 1650–1666, https://doi.org/10.1175/JPO2771.1, publisher: American Meteorological Society Section: Journal of Physical Oceanography.

Skamarock, W. C., 2004: Evaluating Mesoscale NWP Models Using Kinetic Energy Spectra. *Monthly Weather Review*, **132 (12)**, 3019–3032, https://doi.org/10.1175/MWR2830.1.

Soufflet, Y., P. Marchesiello, F. Lemarié, J. Jouanno, X. Capet, L. Debreu, and R. Benshila, 2016: On effective resolution in ocean models. *Ocean Modelling*, **98**, 36–50, https://doi.org/10.1016/j.ocemod.2015.12.004.

Tulloch, R., J. Marshall, C. Hill, and K. S. Smith, 2011: Scales, Growth Rates, and Spectral Fluxes of Baroclinic Instability in the Ocean. *Journal of Physical Oceanography*, **41 (6)**, 1057–1076, https://doi.org/10.1175/2011JPO4404.1.

Uchida, T., and Coauthors, 2021: xgcm/xrft: v0.3.1-rc0. Zenodo, URL https://doi.org/10.5281/zenodo.5503856, https://doi.org/10.5281/zenodo.5503856.

Visbeck, M., J. Marshall, T. Haine, and M. Spall, 1997: Specification of Eddy Transfer Coefficients in Coarse-Resolution Ocean Circulation Models. *Journal of Physical Oceanography*, **27 (3)**, 381–402, https://doi.org/10.1175/1520-0485(1997)027<0381:SOETCI>2.0.CO;2.

von Storch, J.-S., C. Eden, I. Fast, H. Haak, D. Hernández-Deckers, E. Maier-Reimer, J. Marotzke, and D. Stammer, 2012: An Estimate of the Lorenz Energy Cycle for the World Ocean Based on the STORM/NCEP Simulation. *Journal of Physical Oceanography*, **42 (12)**, 2185–2205, https://doi.org/10.1175/JPO-D-12-079.1.

Wunsch, C., and R. Ferrari, 2004: Vertical Mixing, Energy, and the General Circulation of the Oceans. *Annual Review of Fluid Mechanics*, **36 (1)**, 281–314, https://doi.org/10.1146/annurev.fluid.36.050802.122121.

Youngs, M. K., A. F. Thompson, A. Lazar, and K. J. Richards, 2017: ACC Meanders, Energy Transfer, and Mixed Barotropic–Baroclinic Instability. *Journal of Physical Oceanography*, **47 (6)**, 1291–1305, https://doi.org/10.1175/JPO-D-16-0160.1.

Zanna, L., P. Porta Mana, J. Anstey, T. David, and T. Bolton, 2017: Scale-aware deterministic and stochastic parametrizations of eddy-mean flow interaction. *Ocean Modelling*, **111**, 66–80, https://doi.org/10.1016/j.ocemod.2017.01.004.

Zhao, D., and H. Aluie, 2018: Inviscid criterion for decomposing scales. *Physical Review Fluids*, **3 (5)**, 054 603, https://doi.org/10.1103/PhysRevFluids.3.054603.